JGR Space Physics

RESEARCH ARTICLE
10.1029/2025JA034020

Searching for Universality of Turbulence in the Earth's Magnetosphere

Dariusz Wójcik[1,2] and **Wiesław M. Macek**[1,2]

[1]Space Research Centre, Polish Academy of Sciences, Warsaw, Poland, [2]Institute of Physical Sciences, Faculty of Mathematics and Natural Sciences, Cardinal Stefan Wyszyński University, Warsaw, Poland

Key Points:

- Universal Markovian properties of turbulence confirmed across 10 day- and night-side magnetospheric regions using *MMS* data
- Asymmetry found between day- and night-side turbulence, with local physics driving region-specific behavior
- Stationary Fokker-Planck solutions accurately reproduce observed Kappa distributions in all magnetospheric plasma regimes

Correspondence to:

D. Wójcik and W. M. Macek,
dwojcik@cbk.waw.pl;
macek@cbk.waw.pl;
http://users.cbk.waw.pl/~macek/

Citation:

Wójcik, D., & Macek, W. M. (2025). Searching for universality of turbulence in the Earth's magnetosphere. *Journal of Geophysical Research: Space Physics*, *130*, e2025JA034020. https://doi.org/10.1029/2025JA034020

Received 29 MAR 2025
Accepted 2 SEP 2025

Abstract Turbulence in space plasmas remains a fundamental challenge, and Earth's magnetosphere (MSP) offers a natural laboratory for its study. Using high-resolution magnetic field data from the *Magnetospheric Multiscale* (*MMS*) mission, we extend a stochastic Markovian framework to analyze turbulence across 10 diverse magnetospheric regions, including key reconnection sites. We show that magnetic field fluctuations are well described as Markov processes in scale across the kinetic domain. Multi-scale conditional Probability Density Functions (PDFs) reveal Markovian properties beyond the Einstein-Markov scale. The Kramers-Moyal coefficients display linear and quadratic dependencies, and the Fokker-Planck equation accurately reproduces empirical conditional PDFs, with stationary solutions matching observed Kappa distributions. Scale invariance, characterized by power-law behavior and self-similar PDFs, holds up to ∼0.4 s in most regions but breaks in day-side reconnection jets. These findings support the universality of the Markovian cascade description across the magnetosphere, while identifying region-specific deviations that reflect differing energy dissipation mechanisms.

1. Introduction

Turbulence is a prevalent phenomenon in numerous natural systems, particularly in fluids with embedded magnetic fields (Biskamp, 2003; Frisch, 1995), and remains in the ongoing debate within the plasma research community (Matthaeus, 2021). Space and astrophysical plasmas serve as natural laboratories for investigating the turbulent dynamics (Bruno & Carbone, 2016; Chang, 2015). This complex phenomenon encompasses both stochastic and deterministic elements (Echim et al., 2021). Complex systems possess spatial and temporal inhomogeneities, and are composed of many interacting subunits, in which the *nonlinearities* have an important role, so complex spatio-temporal structures appear. Such nonlinear and multi-scale interactions may lead to behaviors not easily predicted knowing only the behavior of individual subsystems. These large-scale emergent behaviors can be either beneficial in facilitating energy transport through the magnetosphere, or detrimental by triggering instabilities that disrupt spacecraft operations and communication systems. It is difficult to comprehensively understand all of complex systems dynamics, so some simplifications and reductions are required (R. Friedrich et al., 2011). The analysis of the systems behavior should be based on the nonlinear mutual interactions and determination of the characteristics of fluctuating forces. This leads to a problem of retrieving a *stochastic dynamical system* from data. The challenging task is to characterize the clearly visible structures of turbulent flows and their variability (Frisch, 1995). In this work, we use the term *structures* to denote the relatively orderly components within complex systems. Mathematical description of structures is the point of interest, and the structures must be linked to some special features of the system.

One particularly challenging case of turbulence is the *small-scale* (kinetic) structure and its deviation from the Gaussian nature (e.g., Alexandrova et al., 2008; Matthaeus, 2021). This deviation is related to the local structure of turbulent flows solution described by Navier-Stokes equations, and to the problem of special small-scale coherent structures, which explain the anomalous statistics (Davidson, 2015). In turbulence theory, *coherent structures* refer to spatially phase-correlated velocities or vortices that span the entire extent of a structure. This phase correlation allows one to determine structural forms through the averaging method, that is troublesome if they are not fixed in a specific location or time. Then one could ask what are the basic features of the complex structures? Most of the approaches concern the statistical structure functions, stochastic and deterministic structures analysis, or linear statistical correlation measures. A standard time series analysis of turbulent data typically includes finding Lyapunov exponents, fixed points, (un)stable limit cycles, or fractal dimensions

(R. Friedrich et al., 2011). However, in such systems, no matter how useful these methods are, the 1- or 2-point statistics may not be enough to fully explain the observed complexity (Peinke et al., 2019).

Therefore, motivated by the requirement of description of turbulent structures, we employ the introductory data and structural analyses, and consider an alternative method which takes advantage of the N-point and N-scale ($N > 2$) joint statistics to provide a broad characterization at arbitrarily many points (R. Friedrich & Peinke, 1997; Macek et al., 2023; Peinke et al., 2019; Strumik & Macek, 2008a, 2008b). General N-scale joint statistics can capture any sequential ordering of any patterns as multi-scale structures, and can be used to find higher-order statistics. In a physical sense, the ordering of N-scale statistics can be seen as a *downward turbulent cascade*, describing interaction between structures from higher to lower scales in a hierarchical manner. This concept can naturally be linked to a phenomenological Richardson (1920) notion of turbulence, which states that a turbulent flow is composed of eddies of varying sizes. Sizes of these eddies define a characteristic *length scale* L, characterized by flow velocity V, and time scales τ that depend on the length scale L. Large eddies, which are inherently unstable, break down to smaller eddies, so the initial kinetic energy is divided into smaller eddies which inherit this energy, and so on. This process continues consistently, with energy being transferred from larger to smaller scales of motion until reaching a sufficiently small length scale, where the viscosity of the fluid dissipates the kinetic energy into internal energy. This final range is called a *dissipation range*. Moreover, the *intermittency* phenomenon, characterized by deviations from such a self-similar cascade process at small scales, is regarded as one of the key signatures of turbulence (Frisch, 1995). In complex systems, such structures often have higher-dimensional forms. However, we presume a simplification of cuts, which may cause the clear structures to somehow deteriorate, but we employ multi-scale statistics to comprehend coherence with respect to higher-order statistics (see also A. Nawroth & Peinke, 2006). The Earth's magnetosphere presents an ideal environment to investigate these turbulence concepts, as it contains regions of vastly different plasma parameters, magnetic field topologies, and energy transfer mechanisms—all accessible through the high resolution spacecraft measurements.

By employing this phenomenological approach, we can analyze how the scale-dependent structures change with scale instead of considering the standard time evolution. Following our previous studies (Macek et al., 2023; Macek & Wójcik, 2023; Wójcik & Macek, 2024), we aim to extend the recent findings of the so-called *Markovian framework* to diverse plasma solar wind regions of the Earth's magnetosphere (MSP) including both day- and night-sides (magnetotail) of the Earth's magnetic field. In such regions some crucial phenomena appear, such as the Electron Diffusion Region (EDR), which initiates the magnetic reconnection process. This Markov framework is known as the *inverse problem* (or more physically a reconstruction method), that is, by taking a data set (time series) and by employing certain parameter estimation techniques, a model is established to describe the dynamics of the underlying process. Such techniques include histogram-based methods, kernel-based estimations, maximum likelihood estimations, statistical moments, or prediction models. On that note, we contribute evidence that the analyzed phenomenological *downward turbulent cascades* have Markovian properties, that is, the processes are memoryless in scale. Next, we propose unified estimates for the Kramers-Moyal (KM) coefficients. We have used a kernel density estimation (KDE) to find the KM coefficients since it is faster and more efficient, than the base histogram-based method (compare Macek et al., 2023), when dealing with relatively smaller data sets. Then we provide the Fokker-Planck (FP) equation in scale, with non-zero drift and diffusion coefficients, for the hierarchical ordering of the N-scale transition statistics. Such an FP equation governs the scale dependence of the conditional Probability Density Functions (cPDFs), and may enable derivation of some other features from scaling behavior to thermodynamics (including a relation to structure functions) (Peinke et al., 2019). We strictly demonstrate that the solution of this equation accurately reproduces the empirical cPDFs in both day-side and night-side selected regions of the MSP. Hence, we aim to show the universality of this data analysis method based on the Markovian nature of the fluctuations in the sub-ion, kinetic domains. Alternatively, one may employ an approach based on the stochastic Langevin equation with the same non-zero drift and diffusion coefficients, which enables the execution of a short-term forecasting procedure (e.g., Peinke et al., 2019).

The presented stochastic multi-scale (and multi-point) approach applied for analyzing the turbulent cascade of the solar wind within the MSP is a phenomenological method. However, the theoretical model of Fokker-Planck (Langevin) equation can be related to various physical systems. Among them we can distinguish, for instance, connection to the Navier–Stokes equations (Laval et al., 2001), the Lundgren hierarchy (J. Friedrich, 2017), nonequilibrium thermodynamics (Peinke et al., 2019), including turbulent flows (Reinke et al., 2018), salient structures of complex systems (Nickelsen & Engel, 2013), or entropies, scale-invariance, and locality (Wójcik &

Macek, 2024) (including a nonextensive Tsallis (1988) entropy). This methodology holds for both microscopic and macroscopic systems.

This study establishes, through multi-scale analysis of NASA's *MMS* mission data, that turbulent magnetic fluctuations in Earth's magnetosphere exhibit universal Markovian cascade properties across diverse plasma regimes, while revealing a critical asymmetry: scale invariance breaks in day-side reconnection jets but persists in night-side magnetotail reconnection. By applying a stochastic framework combining Fokker-Planck equations and structure function scaling analysis, we demonstrate that these statistical signatures correlate with fundamental differences in plasma environment geometry and solar wind coupling. The findings provide new insights into how energy cascades and dissipates in different magnetospheric regions, emphasizing where universal turbulence properties hold and where region-specific physics (such as magnetic reconnection) dominate.

This paper is structured as follows. In Section 2 we present the spacecraft data description, including introductory statistical data analysis, and discuss employed computational methods. Then, in Section 3 we provide and evaluate the plasma parameters and other physical quantities, as well as investigate the power (energy) spectral densities in the inertial and kinetic ranges in all selected regions of the MSP. Next, in Section 4 we introduce the employed methodology, including the stochastic Markovian framework of a turbulent cascade problem in a mathematical manner, and propose the dynamical and stochastic equations at different scales. Consequently, the main results of this paper are presented in Section 5, which is divided into several subsections. We analyze the time series stationarity, examine the power spectra in a frequency domain, then confirm the Markovian character of the $\boldsymbol{B}$-field multi-scale statistics, estimate the unified KM coefficients, compare the derived (generalized) Kappa distributions with the empirical PDFs, and eventually confirm the universal scale invariance in most cases of MSP. Finally, in Section 6 we present the conclusions of our analysis, briefly discus the advantages and limitations of the demonstrated stochastic method, and mention the potential expansion and further development of the Markovian framework.

2. Data Description

The *Magnetospheric Multiscale* (*MMS*) mission began in March 2015 launched by *NASA* (Burch et al., 2016), and still in operation until around 2037 (Burch et al., 2024), has been inspired by the strategy of the *ESA Cluster* mission. It uses four satellites (*MMS* 1–4) in a tetrahedral configuration with identical instruments to observe significant phenomena, for example, the magnetic reconnection and a magnetic turbulence. The *MMS* measures gradients evolving along an equatorial orbit, with considerably small spacecraft separations at electron scales. The instruments also measure plasmas, magnetic and electric fields, velocities, temperatures, and other particles with high time resolution and accuracy. Hence, the *MMS* mission data allows one to study the magnetic reconnections and other plasma instabilities, shock physics, Flux Transfer Events (FTE), flux ropes, and boundary layers, wave and turbulence, plasma jets, Coronal Mass Ejection (CME) impacts on the magnetosphere (MSP), and any other research related to single- and multi-point measurements of the mission. *MMS* observations are perfect for studying kinetic and inertial scale turbulence in the near-Earth space environment.

The main part of this paper consists of the analysis of the *MMS* measurements of a magnetic field strength $\boldsymbol{B} = (B_x, B_y, B_z)$, with the total magnitude $|\boldsymbol{B}| = \sqrt{B_x^2 + B_y^2 + B_z^2}$, in various regions of the MSP. We have selected 10 different time intervals which are displayed in Table 1. We have observations from the *MMS*1-3 satellites (2nd column) from the FluxGate Magnetometer (FGM) sensor (Torbert et al., 2016), of the Burst-type, level L2 scientific data, in the Geocentric Solar Ecliptic (GSE) Cartesian coordinate system. The resolution of these three component $\boldsymbol{B}$-field data is truly high, namely $\Delta t_B = 7.812$ ms, which gives us a sampling frequency of $Fs = 128$ Hz. The 1-D data from *MMS*1–3 instruments were analyzed to isolate temporal scale dependence of magnetic fluctuations. This approach prioritizes continuous 128 Hz sampling over spatial correlations to resolve scale-localized coefficients.

Since we analyze the latest data sets from around 03.2022–12.2023, we note the current operational status of the *MMS* 1–4 instruments (Burch et al., 2024). Most of the instruments are operating nominally, but with a few exceptions (as of July 2024). For *MMS*4 the Fast Electron instruments DES0 and DES1 are non-operational, which are part of the Dual Electron Spectrometer (DES) system. Both are responsible for measuring the energy and angular distributions of fast-moving electrons in the Earth's MSP, and help to investigate physical processes like magnetic reconnection and turbulence. This defect can hinder our ability to fully understand electron-scale

Table 1
List of Selected MMS1-3 Intervals With Calculated Statistics of Turbulent Data

Case	*MMS*	Date	Time begin	End	Location	T_i [%]	*Rng*	*S*	*K*
(a)	1	2023-12-15	22:05:13	22:27:42	MP	20.6	65.1	−2.4	13.7
(b)	3	2023-10-03	20:14:23	20:27:32	QPSC	51.2	39.8	0.53	2.43
(c)	3	2023-06-17	10:27:13	11:00:12	LSMC	22.4	17.3	0.15	2.49
(d)	1	2023-06-13	17:00:23	17:42:32	MSMC	20.2	19.6	−0.7	4.28
(e)	2	2023-02-21	16:39:03	16:56:22	BSW	35.6	8.8	−1.2	2.98
(f)	2	2022-08-19	03:15:23	03:36:43	LEF	70.3	39.6	0.61	2.02
(g)	1	2022-07-11	12:05:23	12:39:33	RCPS	33.7	25.2	−0.1	2.05
(h)	2	2022-05-11	19:35:53	19:44:43	QPBS	37.5	30.8	0.28	1.62
(i)	3	2022-05-04	21:07:33	21:21:32	HSMC	23.1	24.5	−0.4	3.38
(j)	2	2022-03-13	15:59:03	16:53:23	MCRJ	20.1	120.5	−1.9	9.31

processes phenomena. The Dual Ion Spectrometer (DIS) systems are still well operating. The two Active Spacecraft Potential Control (ASPOC) instruments A1E1 of *MMS*2, and A2E3 of *MMS*4 are inactive, meaning that the spacecraft's potential cannot be actively regulated. The uncontrolled potential can affect the accuracy of measurements made by electric field and particle instruments. Since our investigation of the plasma parameters requires observations from these apparatuses, we have limited our analysis to the *MMS*1-3 instruments. Notably, all the magnetic and electric field instruments are still fully operational.

The *MMS* Burst-type instrument has limited capabilities, with only 4% of all data being down-linked daily, so the interval selection criteria must be highly precise. Previously, identification of the near-Earth regions, such as the magnetopause (MP) or magnetosheath (MSH), has been purely based on the gradients in plasma parameters analysis. Now the machine learning algorithms prove to be helpful. To follow the best practices of modern scientific programming, we have employed various open source packages. The machine learning Recurrent Neural Network (RNN) approach presented by Argall et al. (2020), introducing the *MMS* Updated Scientist-in-the-Loop (SITL) Ground Loop System, enables us to search for distinct turbulent (and magnetic reconnection) regions of the MSP with greater precision and speed. Hence, in Table 1 we present all the selected data segments identified using this GLS-MP Python package (see also C. Small et al., 2020; C. R. Small et al., 2020) and the TensorFlow Keras neural network framework (Chollet et al., 2015). Additionally, to study the energy transfer into the MSP, we have employed other open source packages, that is, AstroPy et al. (2022) for the units conversion, PlasmaPy et al. (2024) for the bulk solar wind parameters analysis, and PySPEDAS (Grimes et al., 2022) for the basic time-series and orbit plotting.

Additionally, in Table 1 for all selected regions of the MSP (see exact positions in Figure 1) the spacecraft have been located at geocentric apogee distances of up to $29R_E$ ($R_E = 6371.2$ km). For each sample, the corresponding

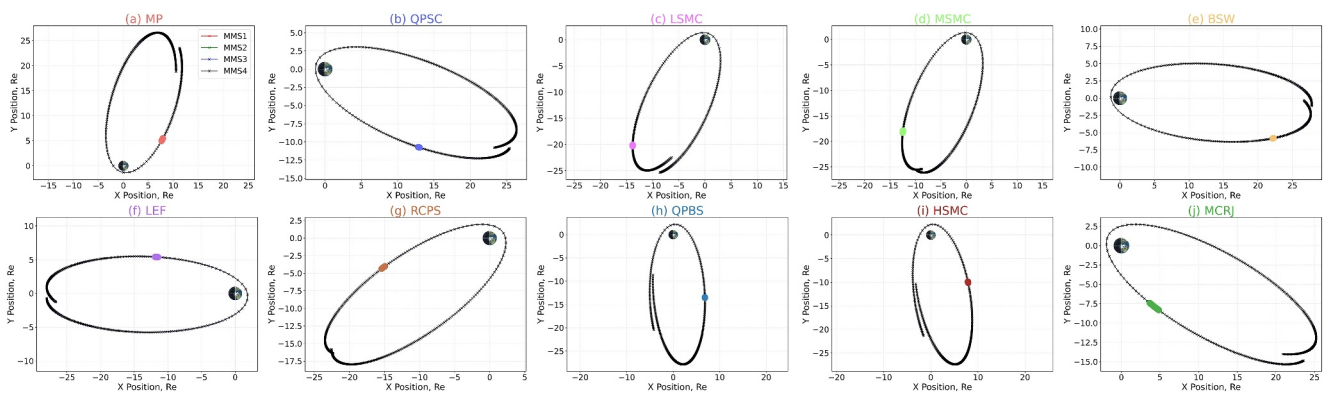

Figure 1. Depiction of the *MMS*1-4 spacecraft orbits in the GSE coordinates in *XY* coordinate plane. Various colored short intervals mark the exact time and location, in Table 1, for each case. Both day-side (on the right) and night-side (on the left) regions of MSP.

Figure of Merit (FOM) ranking is conventionally split into four categories, with values in [0,200]. The predicted encounters of *Sub-Regions of Interest* (SROI) in given locations (abbreviations in 6th column) are as follows: *(a)* MP: low shear MagnetoPause (FOM: 150), *(b)* QPSC: full Quasi-Parallel Shock Crossings (FOM: 130), *(c)* LSMC: long Low Shear MagnetoPause crossing (FOM: 150), *(d)* MSMC: Moderate Shear Magnetopause Crossing with large V_x reversal and small V_z jet and reversal (MP crossing adjacent to dipolarization, FOM: 160), *(e)* BSW: clear Bifurcated Solar Wind current sheet with a reconnection jet (FOM: 150), *(f)* LEF: Large Earthward Flows with turbulent plasmasheet crossings (EDR region, FOM: 180), *(g)* RCPS: Reconnection event, B_z and V_x reversals, Earth-ward to tail-ward flow of 600 km/s, central Plasma Sheet (FOM: 180), *(h)* QPBS: Quasi-Perpendicular Bow Shock (FOM: 110), *(i)* HSMC: High Shear extended MagnetoPause crossing (FOM: 160), *(j)* MCRJ: full Magnetopause Crossing with a Reconnection Jet (FOM: 150).

Since the MP moves back and forth over time, we differentiate between four classes of crossings: partial, low shear, high shear, and complete in cases *(a, c, d, i, j)*. The MP region is interesting since it is a primary location of the mass, momentum, and energy transfer into the MSP. Generally, the MP crossings have similar field and plasma gradients as the bow shock (BS) crossings (cases *(b, h)*), but EDRs exhibit larger amplitude variations than the MP crossings (Argall et al., 2020). Cases *(e, f, g, j)* include selected EDR (and reconnection) regions: at the day-side boundary, where a significant guide field exists; and in the magnetotail, where the $\boldsymbol{B}$-fields are nearly anti-parallel. To identify the reconnection in the day-side (*(e, j)*, of Figure 1) we have checked for large changes in $\boldsymbol{B}$-field components, in $\boldsymbol{E}$-field wave power, and in the electron pressure and ion density. In the magnetotail (*(f, g)* of Figure 1) we have checked the six trigger terms that respond strongly to reversals of $\boldsymbol{B}$ and bulk $\boldsymbol{V}$ (see Argall et al., 2020; Webster et al., 2018).

Next, in Table 1 we see the statistics of turbulent data, which collectively provide insights into the nature of the turbulent plasma and its deviation from Gaussian statistics. In the 7th column we have a turbulence intensity $T_i = \sigma_B/\langle B\rangle$, where σ_B—standard deviation, and $\langle B\rangle$—average value of time series of $\boldsymbol{B}$. It varies significantly, showing differences in the magnetic field's variability relative to its mean strength. In case *(f)* the highest intensity ($T_i = 70.3\%$) indicates high fluctuations in the $\boldsymbol{B}$-field, which is typical of regions with strong Earth-ward flows and turbulent plasma sheet crossings. In case *(j)* the lowest intensity ($T_i = 20.1\%$) corresponds to relatively stable magnetic environment during a full magnetopause crossing, before and after the reconnection event. All values are much higher than $T_i = 17\%$ reported by (Renner et al., 2001). Then, in 8th column we see range *Rng* of data—difference between *max* and *min* values of a sample, which provides a measure of spread or dispersion of data (not definitive due to e.g., extreme values). It gives insights into data outliers and into "wideness" of the data set. In case *(j)* the largest range ($Rng = 120.5$) indicates a substantial spread, possibly due to reconnection-induced large scale magnetic structures. In cases *(c, e)* the smallest ranges (17.3 and 8.8) may reflect more localized or less energetic processes. The 9th and 10th columns show correspondingly the data *skewness S* (3rd-order $\boldsymbol{B}$-field derivative), and *flatness K* (4th-order) of our data sets (see Fuchs et al., 2022). In turbulence framework the skewness and flatness quantify the asymmetry and intermittency of the magnetic gradient distribution, while flatness also diagnoses the intermittency of dissipation scales. According to Kolmogorov (1941) skewness and flatness are independent of the Reynolds numbers Re_λ, but (Kolmogorov, 1962) predicts dependence of flatness on Re_λ, so it is still worth analyzing. Negative S observed in: *(a)* $S = -2.4$ and *(j)* $S = -1.9$ indicates asymmetry favoring the tail of distribution, potentially caused by intense events or jets. Positive S: *(b)* $S = 0.53$ and *(f)* $S = 0.61$ may suggest a dominant forward (or Earth-ward) flows. The $S \notin [-2, 2]$ suggests a non-normality. The flatness varies across cases. High values ($K > 4$): *(a)* $K = 13.7$ and *(d)* $K = 4.28$ reveal highly intermittent turbulence with strong small-scale structures. These regions are likely associated with enhanced energy dissipation. Lower values ($K < 3$): *(g)* $K = 2.05$ and *(h)* $K = 1.62$ indicate less intermittent turbulence, that is consistent with smoother distributions of small-scale gradients. Examining these statistics provides the primary picture of this turbulent environment. Case *(f)* with high T_i and positive S indicates a dynamic region dominated by Earth-ward flows and intermittent structures. While case *(d)* with moderate T_i, but elevated K, shows an intermediate regime where small-scale dissipation plays a prominent role. Thus, we highlight the diverse turbulence characteristics of the selected regions of MSP and their dependence on associated dynamics.

3. Plasma Analysis

By employing the Taylor (1938) *frozen-flow hypothesis* (TH) one can deduce spatial from temporal fluctuations at a single point. This hypothesis assumes the existence of a mean flow, which enables the translation of spatial

Table 2
List of Calculated Plasma and Bulk Solar Wind Parameter Characteristics for the MMS1-3 Interval Samples (Corresponding to Table 1)

Case	$\lvert\boldsymbol{B}\rvert$ [nT]	$\lvert\boldsymbol{T}\rvert$ [eV]	$\lvert\boldsymbol{V}\rvert$ $\left[\frac{\text{km}}{\text{s}}\right]$	$\boldsymbol{V_A}$ $\left[\frac{\text{km}}{\text{s}}\right]$	$\boldsymbol{\beta}$	$\boldsymbol{n_e}$ $\left[\frac{1}{\text{cm}^3}\right]$	$\boldsymbol{n_i}$ $\left[\frac{1}{\text{cm}^3}\right]$	$\boldsymbol{d_e}$ [km]	$\boldsymbol{d_i}$ [km]	$\boldsymbol{\lambda_D}$ [m]	$\boldsymbol{f_{c_e}}$ [Hz]	$\boldsymbol{f_{c_i}}$ [Hz]	$\boldsymbol{T_{\perp e}}$ [eV]	$\boldsymbol{T_{\perp i}}$ [eV]	$\boldsymbol{r_{L_e}}$ [km]	$\boldsymbol{r_{L_i}}$ [km]	$\boldsymbol{f_{\lambda e}}$ [Hz]	$\boldsymbol{f_{\lambda i}}$ [Hz]
(a)	67.43	1073.28	116.09	428.77	0.53	11.79	11.77	2.32	103.88	38.60	1887.54	1.03	103.34	1085.27	0.49	18.28	12.41	1.81
(b)	13.27	205.35	225.77	44.90	1.83	14.88	15.27	1.59	68.91	12.03	371.34	0.20	31.48	194.52	1.83	263.03	23.41	0.54
(c)	10.45	1668.27	175.54	272.63	3.77	0.63	0.70	7.72	312.32	190.92	292.46	0.16	292.42	1655.98	5.66	181.57	4.41	0.68
(d)	13.99	1492.07	214.80	275.57	2.31	1.03	1.22	6.89	269.85	166.66	391.52	0.21	262.34	1496.61	3.83	164.03	5.66	0.90
(e)	6.23	37.61	180.02	47.47	1.81	7.60	8.18	1.93	80.38	11.73	174.35	0.09	18.25	34.76	3.34	956.85	33.20	0.80
(f)	16.77	6969.54	258.73	372.52	6.39	0.43	0.47	1.94	72.09	12.44	469.48	0.26	2798.15	6731.96	20.27	185.46	3.48	0.54
(g)	14.42	1897.28	254.79	88.08	5.63	0.76	0.71	1.17	31.41	8.32	403.62	0.22	315.61	1813.02	5.01	237.29	6.89	0.98
(h)	17.75	99.37	254.91	94.36	2.62	20.77	19.29	1.33	62.53	8.57	496.74	0.27	25.09	91.26	1.01	181.55	31.99	0.71
(i)	18.36	466.14	143.07	172.89	2.97	10.46	10.72	2.92	126.45	30.93	513.86	0.28	47.73	490.28	1.36	95.68	14.49	2.15
(j)	94.09	392.95	167.90	275.25	2.84	61.05	55.55	0.77	34.78	8.15	2633.84	1.43	50.46	428.31	0.28	20.80	41.38	5.81

structures past a stationary probe within a time period shorter than the inherent evolution time of the fluctuations. Taking $|\boldsymbol{V}|$—average flow speed, and τ—scale separation, we have $r = \tau|\boldsymbol{V}|$. However, accuracy of the TH depends on properties of the individual flows and on the statistics being measured.

For instance, Howes et al. (2014) and Klein et al. (2014) have discussed the validity of the TH in context of plasma turbulence, particularly in relation to kinetic Alfvén waves and other plasma phenomena. They have explored the conditions under which TH, which assumes a frozen-in flow for turbulence, breaks down, especially in the dissipation range of plasma turbulence. In the majority of our analyzed events however, we find that the threshold condition for super-Alfvénic flow is not satisfied. This indicates that the plasma dynamics in these intervals are predominantly sub-Alfvénic, suggesting limited available kinetic energy (see again the cases description in Section 2 and Table 2). Such sub-Alfvénic conditions are characteristic of more stable, magnetically controlled environments and may not support typical shock formation or efficient energy dissipation by kinetic processes.

In Table 2, we provide the calculated plasma parameters (corresponding to Table 1), which define characteristics of a plasma, and the bulk solar wind parameters obtained with the *MMS* data (see e.g., Schekochihin et al., 2009). Given that the Burst and FAST-survey data types have different sampling frequencies, we interpolate the $\boldsymbol{B}$-field and DES (electron) data to the DIS (ion) common set of times. For the *MMS* mission the plasma measurements are available at 150 ms for ions and 30 ms for electrons. From the *MMS's* Fast Plasma Investigation (FPI) particles instrument, we calculate the mean total temperature $|\boldsymbol{T}|$ (given $T_{\parallel}$ and $T_{\perp}$), and from the FGM, DES, and DIS instruments we estimate the mean: magnetic field strength $|\boldsymbol{B}|$, ion and electron densities $n_{i,e}$, and ion and electron temperatures $T_{\perp i,e}$. We also compute the $\boldsymbol{E} \times \boldsymbol{B}$ and $V_{\perp}$, so we can calculate the common shock and plasma parameters to describe their global and local behavior across the MSP. We calculate the Alfvén speed from $V_A = \frac{B}{\sqrt{\rho\mu_0}}$, where ρ is the total mass density, and the dimensionless plasma parameter $\beta = \frac{nk_BT}{B^2/2\mu_0}$. When $\beta \gg 1$ the $\boldsymbol{B}$-field is not strong enough to significantly alter the dynamics, so the plasma motion is more gas-like, and when $\beta < 1$ the magnetic tension and magnetic pressure dominate the dynamics. Next, we find the inertial lengths for ions and electrons $d_s = \frac{c}{\omega_{ps}}$, where s is a particle, and ω_{ps} is plasma (angular) frequency. The EDR region should have a characteristic length scale of a few km and be much smaller than the Ion Diffusion Region (IDR). Plasmas are typically quasi-neutral on length scales much greater than the Debye length $\lambda_D = \sqrt{\frac{\epsilon_0 k_B T_e}{n_e q_e^2}}$. We also find the ion and electron gyrofrequencies: $f_{c_s} = \frac{|q_s|B}{2\pi m_s}$ (in Hertz); the relativistic gyroradius for ions and electrons: $r_{Ls} = \frac{\gamma m_s V_{\perp s}}{|q_s|B}$, where $\gamma = \left(1 - \frac{V_{\perp s}^2}{c^2}\right)^{-1/2}$ - Lorenz factor; and the Doppler-shifted characteristic frequency for ions and electrons, related to the respective inertial scales, $f_{\lambda_s} = \frac{V_{\perp s}}{2\pi d_s}$.

The provided data sets reflect diverse solar wind environments, from low-density, higher-speed wind streams (cases *(c, f)*) to dense, slower wind regions (cases *(b, h, j)*). The mean $\boldsymbol{B}$-field strength, spanning 6.23–94.09 nT, shows variability tied to large-scale solar wind structures and local turbulence. In *(j)*, where $|B|$ is particularly

strong, the high magnetic pressure suppresses turbulence, leading to less energy dissipation at small scales (Burlaga, 1995). For weaker fields (case *(e)*) the dynamics become more thermally dominated, consistently with Bruno and Carbone (2016). The plasma β reveals a regime from $\beta = 0.53$ in *(a)* to 6.39 in *(f)*, which is rather typical for these space regions. Low β cases, as in *(a)*, indicate a dominance of magnetic forces, and may favor structures such as flux tubes and Alfvénic turbulence (Schekochihin et al., 2009). High β cases align with observations in regions dominated by thermal pressure, where kinetic effects become pronounced, leading to enhanced turbulence dissipation rates. Trend of higher β in weaker $|\boldsymbol{B}|$ cases may suggest an anti-correlation that has been numerically confirmed in MHD simulations (Matthaeus et al., 1999). The borderline case *(b)*, where $\beta \approx 1$, indicates equipartition between magnetic and thermal pressures, often associated with transitional regions between fast and slow solar wind streams. The Alfvén speed V_A ranges from 44.90 km/s, to 428.77 km/s. High V_A in *(f)* correlates with a strong $\boldsymbol{B}$-field and low plasma density, signifying regions where magnetic waves propagate efficiently, consistently with (Wicks et al., 2010). Then, the low V_A values reflect dense, thermally dominated plasma.

Consequently, the electron and ion inertial lengths $d_{e,i}$ exhibit similar trends, given their dependence on plasma density. Cases with low densities, in *(f)*, show high $d_{e,i}$ indicative of weakly collisional plasmas. These larger inertial lengths suggest enhanced kinetic-scale activity, where non-MHD effects become relevant. Conversely, dense plasma cases, in *(j)*, demonstrate small $d_{e,i}$, consistent with the insight that turbulence is constrained to fluid-like scales. The Debye length λ_D also varies significantly. In case *(c)*, the Debye length λ_D is larger, which suggests a plasma where Coulomb interactions are weaker - this typically occurs in low-density or high-temperature plasmas. The smaller λ_D, in case *(j)*, indicates stronger charge screening, which is characteristic of dense plasmas where electrostatic interactions are more effectively suppressed. For a detailed discussion on deviations from classical plasma predictions, with similar results see for example (F. F. Chen, 2016). The λ_D correlates positively with T_e and inversely with n_e, which reflects the sensitivity of charge screening scales to thermal and density fluctuations in the solar wind. The gyrofrequencies $f_{c_{e,i}}$ and Larmor radii $r_{L_{e,i}}$ reveal insights into particle motion across the cases, for instance, in *(j)* $f_{c_e} = 2633.84$ Hz, reflecting dominance of a strong $\boldsymbol{B}$-field, while $r_{L_e} = 0.28$ km demonstrates tight electron gyration. In contrast, in weak magnetic fields like in *(e)*, f_{c_e} and r_{L_e} are reduced, indicating looser particle gyromotion. These trends align well with gyrokinetic theory (Schekochihin et al., 2009), which predicts such dependencies on $|\boldsymbol{B}|$ and particle velocity. The $r_{L_{e,i}}$ also provide critical benchmarks for kinetic-scale turbulence, with larger gyroradii signaling the transition to inertial range dissipation, a trend observed in spacecraft data (Alexandrova et al., 2008). These statistical and physical trends are consistent with prior works, and provide broader understanding of solar wind dynamics, enhancing our grasp of space plasma turbulence. More precisely, while our observations reveal systematic variations in $|\boldsymbol{B}|$, plasma β, Alfvén speed, and length scales across regions, these trends align well with prior statistical surveys of magnetospheric turbulence (C. H. K. Chen et al., 2014; Leamon et al., 1998; Vech et al., 2018). Rather than replicating the existing parameter-space analyses, given the extensive literature (Howes, 2024; Verscharen et al., 2019), in this paper we would like to focus on how these variations contextualize our novel *Markovian* results based on the *MMS* data (see also Afshari et al., 2024; C. H. K. Chen et al., 2019; Roy et al., 2022), and prioritize the universality aspects presented in the subsequent sections. We extend these foundational studies by quantifying how *Markovian* universality emerges despite the parameter variations documented in prior literature.

4. Mathematical Methods

The *small-scale* (*kinetic*) *structure* of fully developed turbulent flows is considered to represent a universal state defined by statistical stationarity, homogeneity, and isotropy. Physically, this state is characterized by the presence of an energy flux, which is injected into for example, the fluid motion at larger scales and is continuously transported to smaller scales caused by the inherent instability of vortices of a scale τ to perturbations on smaller scales. This process, known as the *turbulent cascade*, describing the small-scale structure of turbulence, is typically studied through the statistics of magnetic, electric field, velocity fluctuations, or any other macroscopic variables (R. Friedrich et al., 2011; Risken, 1996).

We suppose a *complex structure* in space x and time t is given by some physical quantity $u(x,t)$, such that $\delta u(x,t) = e[u(x + er,t) - u(x,t)]$, where e is a unit vector in a direction along which spatial increments are computed (Renner et al., 2001). Using a Taylor (1938) frozen-flow hypothesis, one can assume that temporal and spatial structures are statistically similar. However, both analyses yield equivalent results whether they are

conducted in space or time, in this case we can stay with temporal time scales only. Assume that only one direction e is of interest and that the defining physical quantity is a scalar $u(t)$. We consider the statistics of relative changes from many-to-one point in time of the total magnetic field magnitudes $B = |\boldsymbol{B}|$. Taking $B(t)$ with a fixed $t > 0$, we introduce the time scale $\tau_i := t_i - t$, for $i = 1, \ldots, N$, giving time differences. Then the (left-justified) *fluctuations/increments* of the magnetic field magnitude $\boldsymbol{B}$ are:

$$b_{\tau,i}(t) := B(t + \tau_i) - B(t). \tag{1}$$

for $i = 1, \ldots, N$, which describe the turbulent system (Macek et al., 2023; Macek & Wójcik, 2023). Magnetic field fluctuations are used in turbulence as a proxy of the amount of energy that is contained at a given scale τ into the system. We also consider $b_i := B(t) - |B|$, where $|B|$ is a mean magnetic field magnitude, for multi-point statistics (to differentiate from multi-scale statistics). For the alternative right-justified approach assuming the spatial structures see (Peinke et al., 2019, Figure 2 hierarchical ordering), and for the centered approach see (R. Friedrich et al., 1998; Marcq & Naert, 2001).

The increments Equation 1 highlight the effects of scales of the order of separation τ. It is still compelling to inspect if the analyzed cascade exhibits statistical *self-similarity* and *scale-invariance* behavior (see Belardinelli et al., 2024; Benella et al., 2023). When τ is scaled by a dilation parameter $\lambda \in \mathbb{R}^+$, then the increments are globally *scale-invariant* if scaling occurs with the unique scaling exponent β, that is $b_{\lambda\tau,i}(t) = \lambda^\beta b_{\tau,i}(t)$, with β independent of τ_i. If these fluctuations exhibit global scale invariance, larger structures gradually divide into progressively smaller structures. When this process is homogeneous, each structure decays in the same way (Kiyani et al., 2009). If the quantities $b_{\tau,i}(t)$ and $\lambda^\beta b_{\tau,i}(t)$ have the same statistics, they are called (strictly) *self-similar*.

The Power Spectral Densities (PSDs) serve as a statistic to scrutinize the *scale*-dependent behavior of turbulent fluctuations and are analogous to examining autocorrelation function. Solar wind turbulence description also focuses on the analysis of the mean (absolute) n-th order *structure function*, given by:

$$S_n(\tau) = \langle b_\tau(t)^n \rangle = \frac{1}{N} \sum_{i=1}^{N} |b_{\tau,i}(t)|^n, \tag{2}$$

where n—moment's order, and N—sample size. Hence the $S_n(\tau)$ displays a power-law *scaling* behavior $S_n(\tau) \sim \tau^{\zeta_n}$. However, in the case of a (downward) turbulent cascade as postulated by Landau and Lifshitz (1987), the scaling exponents ζ_n exhibit multifractal scaling behavior, due to highly intermittent nature of the energy dissipation rate. For the energy cascade, this intermittency is directly linked to non-homogeneity of the energy transfer or dissipation rate. This implies that the efficiency of the energy cascade depends on space and time. Scaling behavior, whether linear (fractal) or nonlinear (multifractal), can be verified by experimentally (Frisch, 1995; Renner et al., 2001). However, the (multi)fractal approach focuses on the statistics of the measure $b_\tau(t)$ at a single τ, while for a complexity of the turbulent cascade we want to consider multiple scales $\tau_i \; \forall_i$.

Turbulent cascade can be characterized by various methods, such as by differential equations in variables b_τ and τ; by self-similar structures, that is, fractals or multifractals; or by the Probability Density Functions (PDFs) $P(b_\tau, \tau)$ of b_τ on scales τ (equivalent to structure functions). We want to analyze the multi-scale statistic, that is a probability of finding a sequence of events $b_{\tau,i}$ for scales $\tau_i \; \forall_{i=1,\ldots,N}$. A more engaging quantity though is a conditional probability of obtaining the value $b_{\tau,1}$ at one specific point under the condition of the remaining events. Then, a turbulent cascade can be viewed as a *stochastic process*, governed by the N-scale joint (transition) conditional Probability Density Function (cPDF): $P(b_{\tau,1}, \tau_1 \mid b_{\tau,2}, \tau_2; \ldots; b_{\tau,N}, \tau_N)$ with $P(b_{\tau,i}, \tau_i \mid b_{\tau,j}, \tau_j) = \frac{P(b_{\tau,i}, \tau_i \; ; \; b_{\tau,j}, \tau_j)}{P(b_{\tau,j}, \tau_j)}$, for $\tau_1 < \tau_2$, being conditional PDF, the two-scale joint PDF: $P(b_{\tau,i}, \tau_i; b_{\tau,j}, \tau_j)$, and a marginal PDF: $P(b_{\tau,j}, \tau_j)$. For the downward turbulent cascade the smaller scales τ_i are nested inside the larger scales τ_{i+1}, so we consider the hierarchical ordering of the increments $(b_{\tau,i})_i$ as scale dependent fluctuations moving from larger to smaller scales. Using a Bayes theorem $P(b_{\tau,i}, \tau_i \mid b_{\tau,j}, \tau_j) = \frac{P(b_{\tau,j}, \tau_j \mid b_{\tau,i}, \tau_i) \; P(b_{\tau,i}, \tau_i)}{P(b_{\tau,j}, \tau_j)}$, for $P(b_{\tau,j}, \tau_j) \neq 0$, the reasoning can be inverted (Wójcik & Macek, 2024).

We also note a difference between the multi-point and multi-scale statistics (see also Peinke et al., 2019). The $(N + 1)$-point statistics are noted by $P(b_1, b_{\tau,1}, \ldots, b_{\tau,N})$, or $P(b_{\tau,1}, \ldots, b_{\tau,N}, b_N)$, while the N-scale statistics are

denoted by $P(b_{\tau,1},\dots,b_{\tau,N})$, in terms of scale-dependent increments $b_{\tau,i}$, following Equation 1. If the cPDFs are independent of b_i, then $P(b_{\tau,i} \mid b_{\tau,i-1};b_N) = P(b_{\tau,i} \mid b_{\tau,i-1})$, but there exist experimental evidence that $b_{\tau,i}$ depend on $B(t)$ itself (see e.g., Sreenivasan, 2004). From multi-point statistics one can derive the multi-scale statistics using certain coordinate transformations, but it does not hold in reverse (A. P. Nawroth et al., 2010). For instance, even a simple fluctuation of Equation 1 can be referred to as 1-scale or 2-point statistic in scale. All the following equations, which are presented for N-scale statistics, can be rewritten in the form of $(N+1)$-point statistics, by conditioning on one additional variable (see Stresing & Peinke, 2010).

Consider a dynamical *complex system* with state at time t represented by $X(t)$. If the state of this system at initial t_0 is known, given by $X(t_0) = x_0$, the $X(t)$ is a random variable, for $t > t_0$, and probability of $X(t)$ at successive instants $t_0,\dots,t_N$ is given by N-scale joint cPDF: $\mathbb{P}(X_{t_i} \in [x_i, x_i + dx_i)\ \forall_{i=0,\dots,N} : X_{t_0} = x_0 \quad \text{for } t_0 \le \dots \le t_N)$, then $X(t)$ is a *stochastic process*. We convert the stochastic process $X(t)$ to a process in scale $X(\tau)$, and this stochastic variable $X(\tau)$ is a turbulent increment of the B-field magnitudes in scale τ. Thus, $b_\tau \equiv X_\tau$ is a stochastic variable and $(b_{\tau,i})_i$ defines a *stochastic process*. This introduces the *Markovian framework* for investigation of evolution of cPDFs and the joint statistical properties of fluctuations on scales. If $(b_{\tau,i})_i$ is a stationary process, then this process is *Markovian* if the N-scale joint cPDF is *memoryless*, given:

$$P(b_{\tau,1},\tau_1 \mid b_{\tau,2},\tau_2;\dots;b_{\tau,N},\tau_N) = P(b_{\tau,1},\tau_1 \mid b_{\tau,2},\tau_2), \tag{3}$$

for $0 < \tau_1 < \tau_2 < \dots < \tau_N$. Stochastic process is *memoryless* if the most recent conditioning, say $(b_{\tau,2},\tau_2)$, completely determines transition probability from present to next state of the process. If Markov condition is fulfilled, then using a Bayes theorem, it is fulfilled in the other direction (Renner et al., 2001). Then using definition of N-scale joint cPDF and a memoryless property of Equation 3, we get a relation for the joint N-scale PDF:

$$\begin{aligned} P(b_{\tau,1},\tau_1;\dots;b_{\tau,N},\tau_N) &= P(b_{\tau,1},\tau_1 \mid b_{\tau,2},\tau_2)\, P(b_{\tau,2},\tau_2 \mid b_{\tau,3},\tau_3)\ \cdot \\ &\cdot\dots\cdot P(b_{\tau,N-1},\tau_{N-1} \mid b_{\tau,N},\tau_N)\cdot P(b_{\tau,N},\tau_N). \end{aligned} \tag{4}$$

Having $P(b_{\tau,N},\tau_N)$ and $P(b_{\tau,m},\tau_m \mid b_{\tau,m+1},\tau_{m+1})$ one can describe Markov processes. From Equation 3 we know that the Markov property corresponds to a 2-increment closure for the joint multi-scale statistics. However, the two fluctuations $b_{\tau,1}$ and $b_{\tau,2}$ are considered for three magnetic field values, at three time scales, hence the Markov property is also a 3-scale closure of a general N-scale joint PDF of Equation 4. Empirical evidence shows that the Markov property can hold for the turbulent cascade from the Einstein-Markov scale $\tau_{EM} \approx 0.9\lambda_T$ (λ_T—Taylor length scale) which suggests that molecular friction causes the break-down of the Markov assumption (Lück et al., 2006). Notably, in collisionless plasmas the Taylor scale λ_T reflects kinetic dissipation processes rather than molecular viscosity (see Roberts et al., 2024; Weygand et al., 2009, and references therein). For instance, Matthaeus et al. (2008) demonstrates that in MSP plasmas correlates with d_i and r_{L_e}, not Kolmogorov-like viscous scales.

By integrating over one quantity, say $b_{\tau,2}$ for $\tau_1 < \tau_2 < \tau_3$, and using a memoryless property, from Equation 4 we obtain the generalization of Equation 3 called the *Chapman-Kolmogorov* (CK) *equation* (Risken, 1996):

$$P(b_{\tau,1},\tau_1 \mid b_{\tau,3},\tau_3) = \int_{-\infty}^{+\infty} P(b_{\tau,1},\tau_1 \mid b_{\tau,2},\tau_2)\cdot P(b_{\tau,2},\tau_2 \mid b_{\tau,3},\tau_3)\, db_{\tau,2}, \tag{5}$$

where (τ_1,τ_2,τ_3)—set of time scale parameters. It is a *necessary* requirement for a stochastic process to be *Markovian* (Renner et al., 2001), though it is not *sufficient* (Peinke et al., 2019). Markovianity can explicitly be studied by testing the memoryless property of the Equation 3. This complementary condition is important, since the non-Markovian processes fulfilling the CK Equation 5 exist (see e.g., R. Friedrich & Peinke, 1997; Tutkun & Mydlarski, 2004). For higher-order problems, alternative Markov test methods are available including conditional characteristic functions (B. Chen & Hong, 2012), copula-based characterization (Ibragimov, 2009), or random forest algorithms (Shi et al., 2020).

One can obtain the equation for evolution of the transition PDF from the CK Equation 5, called the *Kramers-Moyal* (KM) forward expansion, given by Risken (1996):

$$-\frac{\partial P(b_\tau,\tau \mid b_{\tau'},\tau')}{\partial \tau}=\sum_{k=1}^{\infty}\left(-\frac{\partial}{\partial b_\tau}\right)^k\left(D^{(k)}(b_\tau,\tau)\,P(b_\tau,\tau \mid b_{\tau'},\tau')\right), \tag{6}$$

where the coefficients $D^{(k)}(b_\tau,\tau)$, called *Kramers-Moyal* (KM) coefficients are:

$$D^{(k)}(b_\tau,\tau)=\frac{1}{k!}\lim_{\tau-\tau'\to 0}\frac{1}{\tau-\tau'}M^{(k)}(b_\tau,\tau,\tau'), \tag{7}$$

$$M^{(k)}(b_\tau,\tau,\tau')=\int_{-\infty}^{+\infty}(b_{\tau'}-b_\tau)^k\,P(b_{\tau'},\tau' \mid b_\tau,\tau)\,db_{\tau'}. \tag{8}$$

The first minus of Equation 6 is due to evolution of scales from larger to smaller ones. We observe that each KM coefficient of order k is just a derivative of the conditional moment of same order (with the exception of a multiplicative constant $1/k!$). The *errors* of the $M^{(k)}$ coefficients, essential for calculating the errors of linear interpolation of the corresponding conditional moments in the KM coefficient as functions of τ', are given by: $\sigma^2_{M^{(k)}}(b_\tau,\tau')=M^{(2k)}(b_\tau,\tau')-\left(M^{(2k)}(b_\tau,\tau')\right)^2$.

The Markovian framework is an extension of the multifractal description of stochastic processes (see e.g., R. Friedrich et al., 2011), thus we note a bridge between these both approaches from the KM expansion (Equation 6) taking the unconditional PDFs. By multiplying with $b^n_\tau(t)$ and integrating with respect to $b_\tau(t)$ the n-th order *structure function* is:

$$\begin{aligned}-\frac{\partial S_n(\tau)}{\partial \tau}&=\sum_{k=1}^{\infty}(-1)^k\int_{-\infty}^{\infty}b^n_\tau\left(\frac{\partial}{\partial b_\tau}\right)^k\left(D^{(k)}(b_\tau,\tau)\,P(b_\tau,\tau)\right)\\&=\sum_{k=1}^{n}\frac{n!}{(n-k)!}\int_{-\infty}^{\infty}b^{n-k}_\tau\left(D^{(k)}(b_\tau,\tau)\,P(b_\tau,\tau)\right).\end{aligned} \tag{9}$$

The structure function $S_n(\tau)$ is well defined and closed solely if the contributions in b_τ are linear for the first KM coefficient, and quadratic for the second-order coefficient.

As we have previously argued (see Macek & Wójcik, 2023) the $M^{(k)}(b_\tau,\tau,\tau')$ coefficients can be obtained from empirical data, while $D^{(k)}(b_\tau,\tau)$ cannot—only by extrapolation in the limit $\tau-\tau'\to 0$. Here we employ a piecewise linear regression with breakpoints (rather than simple linear regression), allowing us to capture potential structural changes in the analyzed relationships. The optimal number and positions of these breakpoints are assessed by the Akaike (1973) and Bayesian (Schwarz, 1978) information criterions (see also Wójcik & Macek, 2024). This effectively serves as an optimal model-selection analysis of this procedure. Then, by systematically varying the range over which we can perform linear fits (varying scales Δt down to 128 Hz), we observe how the estimates stabilize at this smallest scale, confirming the robustness of our extrapolation approach. (see e.g., Roberts et al., 2024, Figure 5). This ensures both numerical stability and optimal structural identification. The small-step approximation, for which $M^{(k)}(b_\tau,\tau,\tau')=D^{(k)}(b_\tau,\tau)\tau'+\mathcal{O}(\tau'^2)$, can be achieved by using the lowest spacecraft sampling rate Δt (Macek et al., 2023): $D^{(k)}(b_\tau,\tau)=\frac{1}{k!}\frac{1}{\Delta t}M^{(k)}(b_\tau,\tau,\tau')$. However, other meaningful approximations and corrections also exist (see e.g., Honisch & Friedrich, 2011; Lehle, 2011).

For a general stochastic process and in most physical applications 1st and 2nd order KM Equation 6 are non-zero and statistically significant, while 3rd and higher-order coefficients gradually approach zero. However examples of non-zero 4th order coefficients are known (see R. Friedrich et al., 2011; Tutkun & Mydlarski, 2004; Tabar, 2019; Wójcik & Macek, 2024). This is summarized by the *Pawula's* theorem (Risken, 1996). If (a) $D^{(k)}(b_\tau,\tau)=0$, for $k\geq 2$, then processes are deterministic (e.g., Ornstein-Uhlenbeck process); (b) $D^{(k)}(b_\tau,\tau)=0$, for $k\geq 3$, then process is limited to 2nd order and is statistically continuous, which results in the

Fokker-Planck equation; (c) $D^{(k)}(b_\tau,\tau)\neq 0\ \forall_{k\in\mathbb{N}}$, then any truncation at order $k\geq 3$ would give non-positive PDFs. From the Pawula's theorem we have the *Fokker-Planck* equation (Risken, 1996):

$$-\frac{\partial P(b_\tau,\tau|b_{\tau'},\tau')}{\partial\tau}=-\frac{\partial}{\partial b_\tau}D^{(1)}(b_\tau,\tau)\,P(b_\tau,\tau\mid b_{\tau'},\tau')+\frac{\partial^2}{\partial b_\tau^2}D^{(2)}(b_\tau,\tau)\,P(b_\tau,\tau\mid b_{\tau'},\tau'),\tag{10}$$

where the $D^{(1,2)}(b_\tau,\tau)$ coefficients are called *drift* and *diffusion* processes respectively. The marginal $P(b_\tau,\tau)$ has to obey the same FP equation. From FP Equation 10 a bridge between multifractal approach and *Markov framework* is obtained: If the KM expansion (Equation 6) shortens to FP Equation 10, then the structure functions are given:

$$-\frac{\partial S_n(\tau)}{\partial\tau}=n\left\langle b_\tau^{n-1}(t)\,D^{(1)}(b_\tau,\tau)\right\rangle+n(n-1)\left\langle b_\tau^{n-2}(t)\,D^{(2)}(b_\tau,\tau)\right\rangle\tag{11}$$

The FP Equation 10 can be rewritten in the expanded form (see Equation 9 of Macek et al., 2023) of 2nd order parabolic PDE. Hence, the *master curve* for invariant PDF of this equation can be evaluated by stationary solution $p_{ST}(b_\tau)$ of FP Equation 10 from $\frac{\partial}{\partial b_\tau}\left[D^{(2)}(b_\tau,\tau)\,p_{ST}(b_\tau)\right]=D^{(1)}(b_\tau,\tau)\,p_{ST}(b_\tau)$. We have (Risken, 1996):

$$p_{ST}(b_\tau)=N_0\exp\left(\int_{-\infty}^{b_\tau}\frac{D^{(1)}(b,\tau)}{D^{(2)}(b,\tau)}db-\ln D^{(2)}(b_\tau,\tau)\right)=N_0\exp(\Phi(b_\tau)),\tag{12}$$

where N_0—integration constant, and $\Phi(b_\tau)$—*potential*. Gradient potential $\partial_{b_\tau}\Phi(b_\tau)$ is interpreted physically as a force of a medium given by the mean field quantities $D^{(1,2)}(b_\tau,\tau)$. The interaction of this force on the path velocity $\partial_\tau b_\tau$ leads to the entropy variation due to the surrounding medium, depending on evolution of $(b_{\tau,i})_i$. Having all these quantities one can find a total *entropy* production collisionless turbulence (see Peinke et al., 2019). For instance, Ewart et al. (2025), through kinetic 1D–1V simulations, showed how stochastic heating cascades energy irreversibly to fine-scale structures in phase space, leading to measurable entropy production. Also, Zhdankin (2023) introduced a generalized entropy framework using Casimir invariants, showing how nonlinear phase-space cascades effectively break these invariants and increase entropy. This supports our interpretation that entropy variations provide meaningful diagnostics for kinetic turbulence processes.

The FP Equation 10 describes a PDF of a stochastic process generated by the complementary *Langevin equation*. Assume that $\Gamma(\tau)$ is δ-correlated Gaussian white-noise, fulfilling normalization: $\langle\Gamma(\tau)\rangle=0$, and $\langle\Gamma(\tau)\,\Gamma(\tau')\rangle=2\delta(\tau-\tau')$ (Risken, 1996). *Cross-correlation* means that assuming an even PDF at larger scales, the stochastic process across scales generates skewness in the PDFs as a result of correlation of additive and multiplicative sources of noise (Laval & Dubrulle, 2006). Then

$$-\frac{\partial b_\tau}{\partial\tau}=D^{(1)}(b_\tau,\tau)+\sqrt{D^{(2)}(b_\tau,\tau)}\,\Gamma(\tau),\tag{13}$$

$$db_\tau=h(b_\tau,\tau)\,d\tau+g(b_\tau,\tau)\,dW_\tau.\tag{14}$$

are *Langevin equations* in partial and stochastic forms, where $h(b_\tau,\tau)=D^{(1)}(b_\tau,\tau)$—*drift* term, $g(b_\tau,\tau)=\sqrt{2D^{(2)}(b_\tau,\tau)}$—*diffusion* term, and $\{W_\tau\mid\tau\geq 0\}$—*Wiener* (Brownian) *process* in scale (Wójcik & Macek, 2024). Memorylessness implies that only δ-correlated noise acts on the trajectory, and the noise has Gaussian distribution (Anvari, Tabar, et al., 2016). Langevin Equation 14 with initial condition can be solved numerically using the *Euler-Maruyama method*. This approximation of a true solution is the Markov process.

5. Results

This section presents a comprehensive stochastic analysis applied to *MMS* data across diverse regions of MSP. We systematically build the case for universal Markovian properties in turbulent cascades, while identifying physically significant exceptions.

5.1. Stationarity

Analysis of time series has a long history in the field of nonlinear dynamics. However, the problem of dynamical noise that is, the fluctuations that interfere with the dynamic evolution has been only briefly addressed (e.g., Anvari, Tabar, et al., 2016). The state of the subsystems of a *complex system* (as mentioned in Section 1) changes over time and result in stochastic dynamics. The dynamics of parameters are generally nonstationary, and the subsystems interact with each other in a nonlinear way. To apply our apparatus, it is essential to meet two fundamental conditions: stationarity of the time series and the Markovian property.

To inspect whether the statistical properties do not change over time, one needs to analyze the *stationarity* of a given data time series. The employed procedure is rather straightforward (Wójcik & Macek, 2024, Appendix A). Firstly, we search for any visible outliers and drifts in data, or trends and seasonality by analyzing the time series. Then we evaluate the hypotheses of the Augmented *Dickey-Fuller* and *Kwiatkowski-Phillips-Schmidt-Shin* tests, with a significance level of $\alpha = 0.05$, which focus on identifying *unit roots* that can indicate stochastic non-stationarity, particularly related to random walks. Then, we use the `lag-1` differencing: $\nabla b(t) = b(t) - b(t-1)$ to obtain stationarity, where ∇—difference operator. For cases with the highest turbulence intensity T_i (see Table 1) we employ the second difference $\nabla^2 b(t) = b(t) - 2b(t-1) + b(t-2)$, which is based on the observation that the autocorrelation function of $b(t)$ exhibited substantial correlations at larger lags. We employ the linear interpolation of neighboring values to fill any empty data points in time series (Macek & Wójcik, 2023). We also removed all the low-significance outliers at the largest $\boldsymbol{B}$-fields.

We note that cases *(e, f, g, j)* include selected EDR (reconnection) regions, which in a physical setting can be determined, for example, by identifying the large changes in $\boldsymbol{B}$- or $\boldsymbol{E}$- fields. These physical sudden changes of magnitude, in a mathematical setting, can be regarded as jumps or discontinuities. Here, the models including jump-term could possibly be favorable (see e.g., Tabar, 2019), however employing the `lag-1` differencing and the standard modeling approach presented in this paper is still suitable.

5.2. Spectral Analysis

To confirm the consistency of analyzed data with the popular characteristics of the small-scale turbulence, in addition to the turbulence intensity T_i analysis, we analyze the scaling of the spectral densities in a frequency domain. As mentioned in Section 4, the Power Spectral Densities (PSDs) serve as a statistic to scrutinize the *scale*-dependent behavior of turbulent fluctuations and are analogous to examining the autocorrelation function. For the spectral analysis we have used the Matlab (R2025a) language, with the open source package developed by Fuchs et al. (2022). Since the authors analyze the velocity time series, certain function modifications have been made to address the differences. We have taken into account the required turbulence-specific (HIT) assumptions, although non-ideal homogeneous turbulence conditions are noticeable in a few cases. Here the 1-D spectrum can be determined by the Fast Fourier Transformation (FFT) of time-varying signals through a single-point measurements. The PSDs can be transformed to Energy Spectral Densities (ESD) by a simple transformation with sampling frequency Fs. Following (Fuchs et al., 2022), we distinguish between: PSD $= |FFT(\text{data})|^2/L_{\text{data}}$, and ESD $= |FFT(\text{data})|^2/(Fs \cdot L_{\text{data}})$, where L_{data}—number of data samples. The *ESDs* are normalized so that $\sigma^2 = \int_0^\infty E(f)df$, where σ^2—variance of the time series and the single-sided spectrum $E(f) = 2\text{ESD}\ (2{:}L_{\text{data}}/2 + 1)$.

This scaling analysis is seen in Figure 2 of the Energy Spectral Densities (ESDs) plots in the frequency domain, with additional averaging (moving average filter), for all data sets. We see again significant variations in turbulent properties across different cases *(a—j)*. The spectra provide information on the energy cascade from large to small scales and the transition from the MHD inertial range to kinetic dissipation range, resulting in dissipation of magnetic and kinetic energy from turbulent fluctuations into particle heating and acceleration, as well as enhanced entropy in the plasma system. The *inertial range* is a large scale interval defined from around energy injection scale to approximately $10d_i$ after which the kinetic scale emerges. Then the dissipation mechanisms are considered in the collisionless regime typical of space plasmas, where particle-wave interactions and magnetic reconnection are dominant. Calculated mean gyrofrequencies f_{c_s} characterize the kinetic regime (in Hz), while mean gyroradiuses r_{Ls} define the kinetic interval (in km). Here, the most cases exhibit a power-law scaling close to the expected Kolmogorov $f^{-5/3}$ spectrum (dashed lines), indicative of well-developed turbulence. The transition to kinetic scales and spectral steepening vary significantly. In cases *(f, g)* we see extended inertial range, with

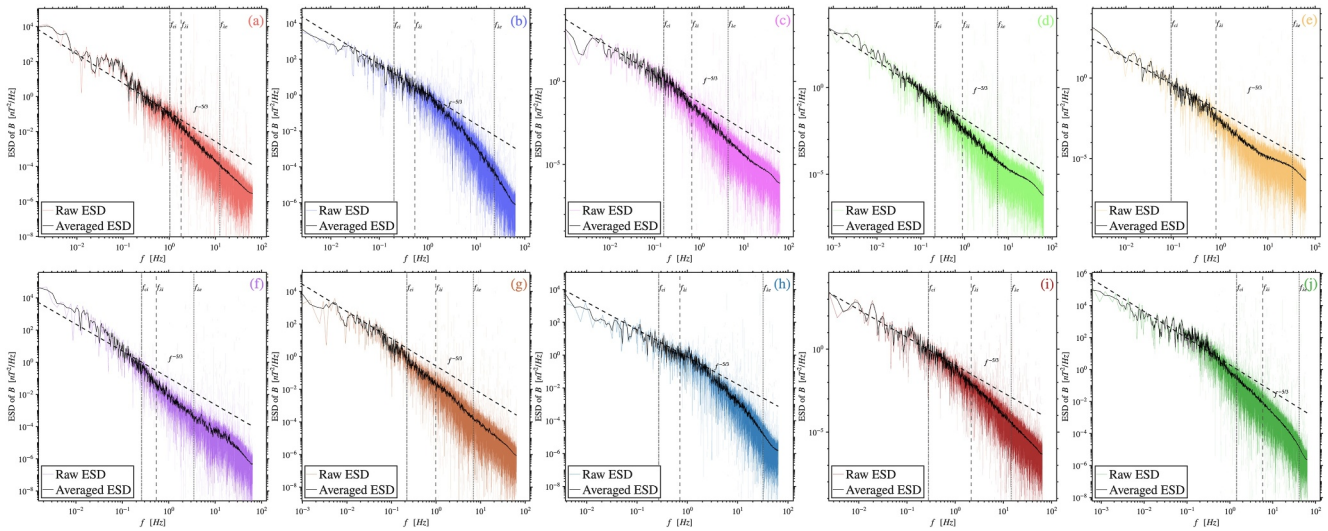

Figure 2. Energy Spectral Densities (ESDs) in the frequency domain, on logarithmic axes, of the high-resolution *MMS*1-3 turbulent data in the MSP. Typical inertial range Kolmogorov spectra of $f^{-5/3}$ are reported with dashed lines. The steeper spectra in the kinetic range, until dissipation scales can also be seen. Data from the MMS mission for $\boldsymbol{B}$ in ten cases (a–j) corresponding to Tables 1 and 2.

spectral break occurring at a higher frequency. This suggests a more efficient energy cascade which is likely facilitated by strong Alfvénic turbulence and higher ion inertial length d_i. This extended range aligns with other studies on solar wind turbulence, where higher Alfvénic activity is correlated with an increased range of energy transfer before dissipation (Bruno & Carbone, 2013; F. F. Chen, 2016). In contrast, cases *(b, j)* exhibit much sharper spectral steepening beyond the inertial range, implying a more abrupt transition to dissipation, consistent with the higher plasma density and electron cyclotron frequency in this region. It could be due to stronger electron damping effects, as it corresponds to a high-density plasma environment with a strong background $\boldsymbol{B}$-field. Such conditions enhance electron Landau damping, which rapidly dissipates energy at small scales (Howes et al., 2008; Sahraoui et al., 2009). Cases *(c, e)* are intermediate scenarios, where the spectral breaks occur at a moderate frequency. It suggests a more balanced interplay between inertial and kinetic scale processes. Given the relatively high β, kinetic instabilities could play a role in modifying the spectral shapes (see e.g., Matthaeus, 2021). For instance, the hybrid-kinetic simulations by Arzamasskiy et al. (2023) show that pressure-anisotropy driven instabilities, for example, firehose and mirror modes, significantly modify turbulence dynamics in high-β plasmas, steepening the energy spectra and regulating anisotropy. The kinetic simulations (Bott et al., 2025) illustrate how whistler-mode heat-flux instabilities efficiently mediate electron scattering and energy dissipation under similar conditions. Thus, the kinetic instabilities can influence spectral shapes observed here, particularly at high β. Then, case *(i)* presents a more gradual spectral transition, suggesting a mixed regime where both Alfvénic and kinetic turbulence mechanisms could simultaneously be active. This comparative analysis of ESDs confirms the presence of well-developed turbulence, with case-dependent variations in spectral evolution. The observed differences in spectral break frequencies and dissipation slopes reinforce the idea that turbulence in space plasmas is highly dependent on local plasma parameters. The results are consistent with previous turbulence studies in the solar wind and MSH, demonstrating the complex interplay between nonlinear energy transfer and kinetic dissipation mechanisms.

5.3. Markovian Properties

Motivated by the cascade picture from the largest to smallest scale, we want to check the hypothesis of Markovian properties of turbulent data (Macek & Wójcik, 2023). Hence, we firstly test the *necessary* CK Equation 5, and then the *sufficient* memoryless property of Equation 3 to qualitatively prove the Markovianity of the process in scale. If the necessary and sufficient conditions are fulfilled then the evolution of cPDFs has to be specified by the stochastic evolution given by KM Equation 6.

For the available turbulent *MMS* data (see again Sections 2 and 3), we can verify both conditions experimentally. The CK condition (Equation 5) can be tested straight from the data, using the integral formula for conditional

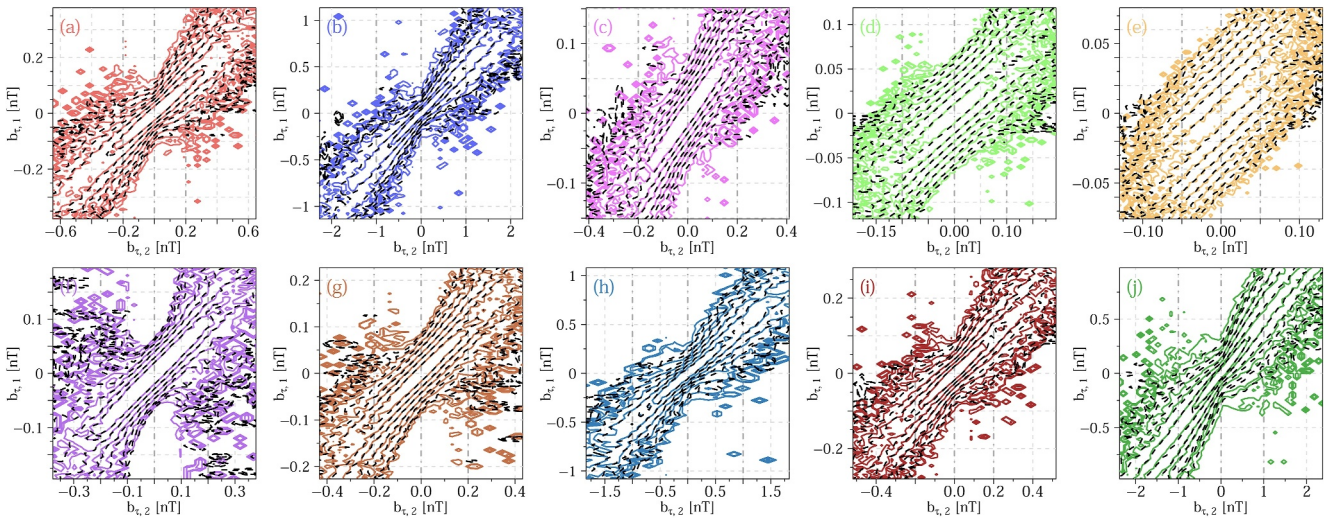

Figure 3. The comparison between empirical single-cPDFs $P(b_{\tau,1},\tau_1|b_{\tau,2},\tau_2)$ (colored curves), and double-cPDFs $P(b_{\tau,1},\tau_1|b_{\tau,2},\tau_2;b_{\tau,3}=0,\tau_3)$ (dashed black curves) for different time-scales. $b_{\tau,3}=0$ is fixed, since for this value we get the peak of the cPDF. *MMS* data for $|\boldsymbol{B}|$ fluctuations. Data from the MMS mission for ten cases (a–j) correspondind to Tables 1 and 2.

densities, while the *memoryless* property of Equation 3 can be verified for $N=3$, that is, for the 3-scale cPDFs: $P(b_{\tau,1},\tau_1 \mid b_{\tau,2},\tau_2) = P(b_{\tau,1},\tau_1 \mid b_{\tau,2},\tau_2;b_{\tau,3},\tau_3)$, $\tau_1<\tau_2<\tau_3$, as described in Section 4. Notably, even a 1-scale PDF $P(b_\tau,\tau)$ can characterize a complex system, and one can find all higher-order moments $\langle b_\tau(t)^n\rangle$ (Frisch, 1995), but one does not have any information about more than 1- or 2-scale correlations. Thus we employ a three-scale cPDFs closure (R. Friedrich et al., 2011).

Since the *necessary* CK condition (Equation 5) has been thoroughly analyzed and proven for various scales in our previous works using *MMS* data (see e.g., contours of Wójcik & Macek, 2024), we refrain from reiterating the analysis in this paper. We affirm though that analogous results are obtained within the broader scope in day- and night-side of MSP in this study. Then, the sufficient *memoryless* property of Equation 3—a three-scale closure simplification can be tested experimentally. By determining different fluctuations for same reference value, we examine cPDFs $P(b_{\tau,1},\tau_1 \mid b_{\tau,2},\tau_2;\ldots;b_{\tau,i},\tau_i)$ of Equation 3. In Figure 3 we test the Markovianity by comparing the empirical single-cPDFs $P(b_{\tau,1},\tau_1 \mid b_{\tau,2},\tau_2)$ (colored curves), and double-cPDFs $P(b_{\tau,1},\tau_1|b_{\tau,2},\tau_2;b_{\tau,3}=0,\tau_3)$ (black curves) for all analyzed cases. Note that we fix $b_{\tau,3}=0$, because for this value the peak of the cPDF is achieved (see also middle parts of Figure 4) and such conditioning makes the 2-D representation feasible. However, the results are notably similar for other selected $b_{\tau,3}$ values. The chosen time scale parameters $\tau_1<\tau_2<\tau_3$ (Section 4) are taken such that $\tau_2=\tau_1+\Delta t_B$ and $\tau_3=\tau_1+2\Delta t_B$, where Δt_B—lowest sampling time of the Burst-type observations from the *MMS's* FGM sensor. Below a certain threshold value of τ the Markov properties are no longer valid, which indicates some structural change, that is, caused by small-scale coherent structures. Hence, we have chosen τ_1 to be $\sim$3 times greater than Δt_B, which gives us a lower-bound scale in relation to the Einstein-Markov scale τ_{EM} (Lück et al., 2006). Below this scale the stochastic process loses its *memoryless* property, and it can be viewed as a scale below which the turbulence is no longer effectively δ-correlated. This corresponds to $(\tau_1,\tau_2,\tau_3)=(0.02,0.0278,0.0356)$ s.

In Figure 3 we also see that the 3-scale cPDFs $P(b_{\tau,1},\tau_1 \mid b_{\tau,2},\tau_2;b_{\tau,3},\tau_3)$ depend on $b_{\tau,2}$ because the contours are not parallel to the $b_{\tau,2}$ axis, so the 3-scale cPDFs cannot be reduced to 2-scale closure of cPDFs. This implies that the features of fluctuations for only 1-scale, which can be done by examining structure functions of Equation 2, are not complete, so a multi-scale approach is statistically correct. Nevertheless, the proximity of two corresponding displayed contours yields evidence for the validity of the 3-scale closure. The close alignment between these contours demonstrates that knowing $b_{\tau,3}$ provides no additional statistical information beyond what is provided by $b_{\tau,2}$. Similarly to the other MSP regions (Macek & Wójcik, 2023), we observe that within the inner core agreement is most pronounced since the statistics converge better due to larger number of samples of the cPDFs. Hence the *memoryless* property of Equation 3 is valid for such time scale set in all the analyzed cases. We have additionally verified that the CK Equation 5 is satisfied for larger scales, approximately up to 50 $\Delta t_B=0.39$

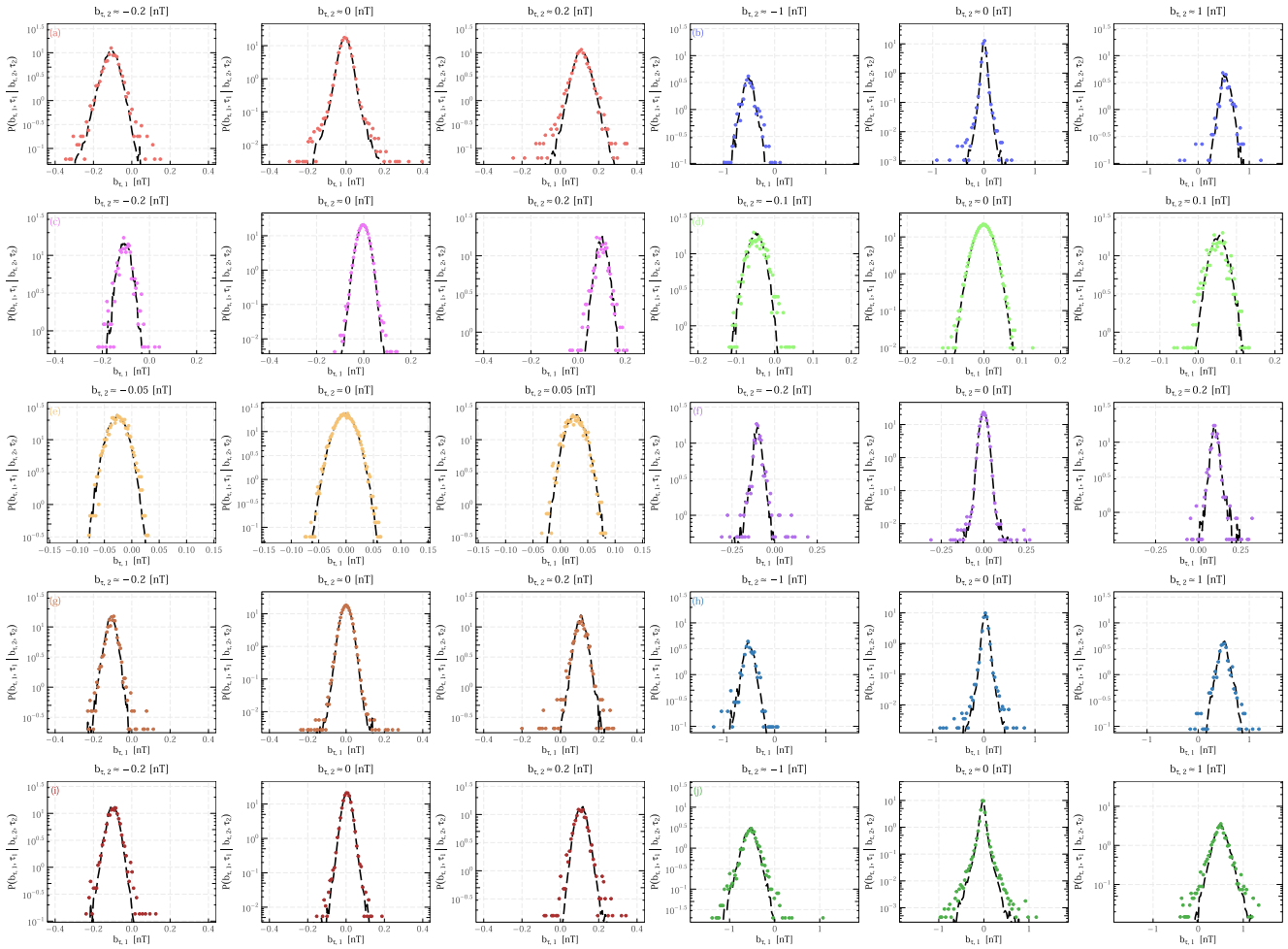

Figure 4. Comparison of the cross sections through the empirical single- and double-cPDFs under fixed magnetic increment $b_{\tau,3}$ for all cases (related to Figure 3). The parameter set (τ_1, τ_2, τ_3) is in agreement with the previous figure.

s, which indicates greater universality in the scale-dependence. If the larger data set on kinetic scales is available, then further larger-scale increments can be investigated, however, the validity of relation Equation 3 is sufficiently strong (see Holstein & Kantz, 2009).

Then, in Figure 4 we have depicted the orthogonal cuts through the cPDFs for the chosen values of parameter $b_{\tau,2}$ (at the top of each plot). As evident, the cuts through the empirical single-cPDFs (colored points) align quite closely with the cuts through double-cPDFs (black curves), resulting in a great fits. Indeed only in a few cases the colored points deviate from the lines in tails, but it appears to be caused by the data outliers and inherent numerical noise. We can conclude then that both *necessary* and *sufficient* conditions of Equations 3 and 5 are fulfilled for the chosen set on small kinetic scales in all considered cases. Notably, while we have shown these results for the multi-scale statistics $P(b_{\tau,1}, \tau_1 \mid b_{\tau,2}, \tau_2; b_{\tau,3}, \tau_3)$, the empirical examinations indicate that the same results hold for the multi-point statistics $P(b_{\tau,1}, \tau_1 \mid b_{\tau,2}, \tau_2; b_{\tau,3}, \tau_3; b_N)$ of turbulent cascade. Analogous results for Markovian turbulence have been showed for other simulations and data sets (see Benella et al., 2022; J. Friedrich, 2017; R. Friedrich & Peinke, 1997; R. Friedrich et al., 1998, 2011; Fuchs et al., 2022; Lück et al., 2006; A. P. Nawroth et al., 2010; Renner et al., 2001; Stresing & Peinke, 2010; Tutkun & Mydlarski, 2004).

5.4. Kramers-Moyal Coefficients and Parametrization

Evolution of $(b_{\tau,i})_i$ has Markov properties, no memory, and is a stochastic process that evolves in scale τ. It is limited though to the time scales greater than the Einstein-Markov scale τ_{EM} (small-scale cutoff) and smaller than the experimentally discovered limits. Thus, a Markov process can be taken as a stochastic process, modeling the

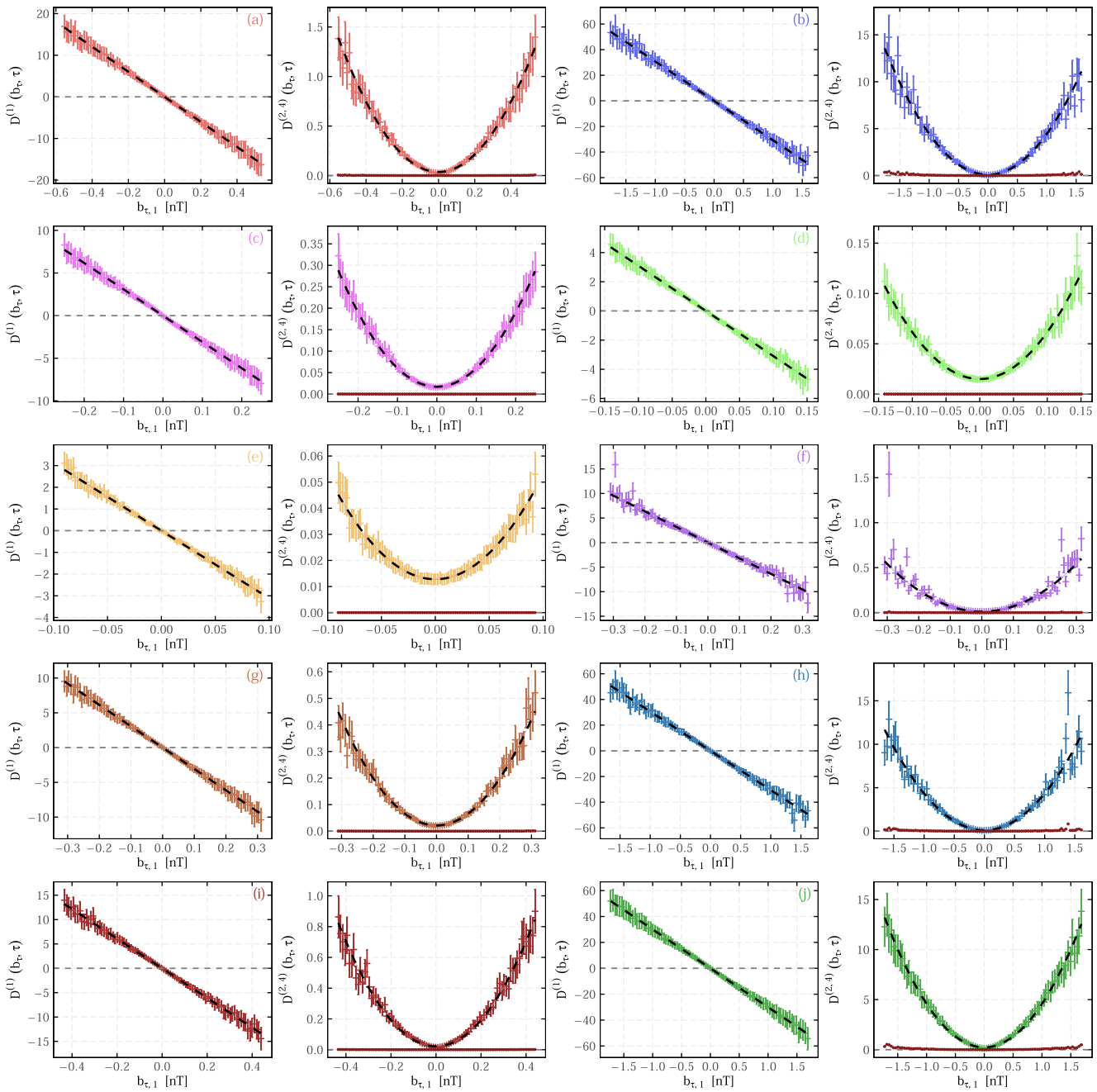

Figure 5. First and second KM coefficients Equation 7 as functions of magnetic increments b_τ, for $B = |\boldsymbol{B}|$. Dashed black lines show optimal fits to empirical values of $D^{(1)}(b_\tau,\tau)$ and $D^{(2)}(b_\tau,\tau)$, with $D^{(4)}(b_\tau,\tau)$—in agreement with the Pawula's theorem. Data in cases (a–j) corresponding to Tables 1 and 2.

coarse-grained process. Using the empirical joint PDFs we find the cPDFs and thereby the equations for conditional moments Equation 8 as functions of b_τ (see also Macek & Wójcik, 2023; Wójcik & Macek, 2024, Appendix B). To derive the KM coefficients (Equation 7) we use a piecewise linear regression with breakpoints. For each conditional moment, we compute values at multiple scale differences, and extrapolate in $\tau - \tau' \to 0$ using weighted linear fits that prioritize smaller scale differences. This approach provides robust extrapolation even with the limited Burst spacecraft data (e.g., Honisch & Friedrich, 2011).

In Figure 5 we see the results of this analysis for the four KM coefficients. We observe that in all cases the non-parametrically obtained point-by-point $D^{(1)}(b_\tau,\tau)$ coefficients have linear dependence on b_τ with some small deviations, while $D^{(2)}(b_\tau,\tau)$ coefficients are 2nd degree polynomials, with slightly larger deviations in a few cases

(e.g., (*f*)). It is clear though that the $D^{(2)}$ coefficient is more affected by experimental noise (especially in tails). The linear shapes of $D^{(1)}$ correspond to deviations of cPDFs from diagonal lines in Figure 3. The consistently linear form of $D^{(1)}$ across all MSP regions indicates a universal restoring force mechanism proportional to fluctuation magnitude, analogous to a damped harmonic oscillator in physical systems. This linear drift term physically represents the tendency of fluctuations to return toward equilibrium through wave dispersion effects. The quadratic $D^{(2)}$ reveals multiplicative random forcing that increases with fluctuation magnitude, consistent with nonlinear wave-wave interactions that intensify for larger-amplitude fluctuations (R. Friedrich et al., 2011). Then, as observed, all $D^{(k)}(b_\tau,\tau) \approx 0,\ k \geq 3$ within the experimental precision, so the *Pawula's* theorem applies. If $D^{(4)} \gtrsim 0$ it is sufficient to examine the ratio of the structure functions $S_4(\tau)$ to $S_2(\tau)$ of Equation 9. If it is small, then the effect of the 4th order term can be neglected, which holds in this study. Hence, the KM expansion (Equation 6) truncates at $k = 2$, and reduces to the FP Equation 10. In terms of the Langevin Equation 14, the physical interpretation of this result is that the noise $\Gamma(\tau)$ acting on the process can be considered as Gaussian distributed in addition to its δ-correlation. Thus we assume a general polynomial parametrization of $D^{(1)}(b_\tau,\tau) = a_1(\tau) + b_1(\tau)\, b_\tau$, and $D^{(2)}(b_\tau,\tau) = a_2(\tau) + b_2(\tau)\, b_\tau + c_2(\tau)\, b_\tau^2$, where a_1, b_1, a_2, b_2, c_2 depend on $\tau > 0$.

However, for several reasons we can simplify it. Firstly, we expect that the PDFs are symmetric with respect to zero. Also, the two additional parameters increase complexity of the solution of FP Equation 10, even if we would assume dependence of coefficients of $D^{(2)}$ on $D^{(1)}$ (see Equations 7 and 8 and (Equations 14 and 15) of Belardinelli et al., 2024). Then, the reduction simplifies the application of structure functions, $\langle b_\tau(t)^n \rangle$, that here become equivalent to the absolute structure functions, $\langle |b_\tau(t)^n| \rangle$, while in the more general approach these two should not be confused. In short this fact can be proven by taking two FP Equation 10, one for $P(b_\tau,\tau)$ and second for $P(-b_\tau,\tau)$, and inserting them to corresponding structure functions. After a few derivations, one can see that these equations will differ in coefficients. Hence, without significant loss of accuracy (see also Reinke et al., 2018) we eliminate the second terms in both $D^{(1)}$ and $D^{(2)}$, and assume a stricter parametrization:

$$\begin{cases} D^{(1)}(b_\tau,\tau) = -b_1(\tau)\, b_\tau, \\ D^{(2)}(b_\tau,\tau) = a_2(\tau) + c_2(\tau)\, b_\tau^2. \end{cases} \tag{15}$$

By conducting a similar reasoning as Macek and Wójcik (2023, Figure 5) of proposed b_1, a_2, c_2 parameters we see that they feature a power-law dependence on scales τ:

$$\begin{cases} b_1(\tau) = A\tau^\alpha, \\ a_2(\tau) = B\tau^\beta, \\ c_2(\tau) = C\tau^\gamma, \end{cases} \tag{16}$$

where the parameters $A, B, C, \alpha, \beta, \gamma \in \mathbb{R}$ can be found experimentally (compare Macek et al., 2023). Since the complete parametric study has been done in our previous papers, we refrain from providing all of the parameters values, and list only the averaged ones. Anyway, these dependencies are just loose parametrizations of the empirical findings, and other theoretical analyses may lead to slightly varying dependencies. We also discern the mostly symmetrical fit of the $D^{(2)}(b_\tau,\tau)$ on b_τ (compare Renner et al., 2001). The results proposed on $D^{(1,2)}$ may be understood as the result of a projection of the high-dimensional problem of turbulence on the subspace of the $\boldsymbol{B}$-field fluctuations.

5.5. Fokker-Planck Modeling and Kappa Distributions

By inserting both KM coefficients (Equation 15) into the FP Equation 12 we retrieve the solution $p_{ST}(b_\tau,\tau)$, which is a PDF of the *Kappa* distribution (Risken, 1996):

$$p_{ST}(b_\tau,\tau) = \frac{\Gamma(\kappa)}{\Gamma\left(\kappa - \frac{1}{2}\right) b_0 \sqrt{\pi\kappa}} \cdot \frac{1}{\left[1 + \frac{1}{\kappa}\left(\frac{b_\tau}{b_0}\right)^2\right]^\kappa}, \tag{17}$$

where $b_0 = \sqrt{\frac{a_2(\tau)}{c_2(\tau)+b_1(\tau)/2}}$—scale parameter, $\kappa = 1 + \frac{b_1(\tau)}{2c_2(\tau)}$—shape parameter (regulating weight of the tails), and $a_2(\tau)$, $b_0(\tau) \neq 0$, while $\Gamma(\kappa) = \int_0^\infty b_\tau^{\kappa-1} e^{-b_\tau} db_\tau$—Gamma function. The κ parameter represents the ratio of additive and multiplicative noise in the diffusion term of the stochastic process. This scale-local Kappa distribution emerges from the FP solutions of temporal Markov processes, independent of a 3-D spatial structuring. This single-point focus enables direct comparison to solar wind studies (Matthaeus et al., 2016), while identifying priority regions (e.g., day-side EDRs) for future multi-scale missions. This distribution is symmetric around zero, with a peaked bell-shape, and approaches Gaussian as $\kappa \to +\infty$ (Macek & Wójcik, 2023). In particular, FP Equation 12 with $D^{(2)}(b_\tau, \tau)$ constant in b_τ has Gaussian solutions. The mean parameter values, obtained through a fitting of the *MMS* data, for smaller scales (up to ∼0.4 s), of the stationary solution Equation 17 are: case *(a)* $\kappa = 1.099$, and $b_0 = 0.357$, *(b)* $\kappa = 1.118$, and $b_0 = 0.834$, *(c)* $\kappa = 1.165$, and $b_0 = 0.122$, *(d)* $\kappa = 1.344$, and $b_0 = 0.083$, *(e)* $\kappa = 1.937$, and $b_0 = 0.085$, *(f)* $\kappa = 1.071$, and $b_0 = 0.238$, *(g)* $\kappa = 1.126$, and $b_0 = 0.178$, *(h)* $\kappa = 1.534$, and $b_0 = 1.276$, *(i)* $\kappa = 1.025$, and $b_0 = 0.241$, and *(j)* $\kappa = 1.247$, and $b_0 = 0.998$. As the scale increases, the κ also increases until reaching a Gaussian distribution in $\kappa \to \infty$, as predicted by theory. Mean $\kappa \approx 1.27$ across data sets indicates strongly non-Gaussian statistics with pronounced tails, with highly intermittent turbulence. Lower κ's represent enhanced probability of large-amplitude fluctuations compared to Gaussian processes. The $\kappa < 1.5$ indicates strong intermittency likely driven by coherent structures such as current sheets (Pavlos et al., 2012). Then the corresponding non-extensivity parameter $q = \frac{b_1}{2c_2+b_1} = \frac{\kappa-1}{\kappa} \approx 0.22$ in generalized Tsallis (1988) mean entropy quantifies the degree of long-range correlations in the system, with higher q values indicating stronger correlations.

Finally, we note that considering a previous broader parametrization of Equation 15, one can derive the *generalized Kappa distribution* with a symmetry parameter λ (see Belardinelli et al., 2024, for Langevin approach). Here, $\lambda = -\frac{b_2(\tau)}{2c_2(\tau)}$, and if $\lambda = 0$, then the distribution is reduced to regular *Kappa* distribution of Equation 17. If $\lambda > 0$ then the left tail of the distribution is higher than the other, and if $\lambda < 0$, the right tail is higher, and nonvanishing odd moments emerge.

Knowing the parametrization of both $D^{(1,2)}(b_\tau, \tau)$ coefficients, the cPDFs can be obtained by the *short time propagator* (Risken, 1996):

$$P(b_\tau, \tau | b_{\tau'}, \tau') \approx \frac{1}{\sqrt{4\pi\tau' D^{(2)}(b_{\tau'}, \tau')}} \cdot \exp\left(-\frac{\left(b_\tau - b_{\tau'} - D^{(1)}(b_{\tau'}, \tau')\right)^2}{4\tau' D^{(2)}(b_{\tau'}, \tau')}\right), \tag{18}$$

where $\tau' = \tau + \tau_{EM}$. This form is reached by implementing the scale step in units of the Einstein-Markov scale, which makes the propagator depend on $D^{(1,2)}(b_\tau, \tau)$ only. Using Equation 18 one can find the cPDFs and compare them with the solutions of conditional FP Equation 10. The experimental cPDFs $P(b_\tau, \tau | b_{\tau'}, \tau')$ become noisy at greater values of b_τ. Then by inserting KM Equation 15 into the FP Equation 10, we get (Macek et al., 2023):

$$\begin{aligned} &\left[a_2(\tau) + c_2(\tau)\, b_\tau^2\right] \frac{\partial^2 P(b_\tau, \tau)}{\partial b_\tau^2} + \left[b_1(\tau) + 4c_2(\tau)\right] \cdot b_\tau \frac{\partial P(b_\tau, \tau)}{\partial b_\tau} + \\ &+ \frac{\partial P(b_\tau, \tau)}{\partial \tau} + \left[b_1(\tau) + 2c_2(\tau)\right] P(b_\tau, \tau) = 0, \end{aligned} \tag{19}$$

which can be solved numerically by Euler integration scheme, has been verified for stationary solution $\partial P(b_\tau, \tau)/\partial\tau \equiv 0$, and agrees well with our previous results. This completes the demonstration of the FP Equation 10 as a model of scale-dependent complexity.

In Figure 6 we compare the stationary (open circles) and non-stationary (gray dashed lines) solutions of the evolution FP Equation 10 with the spacecraft empirical PDFs (colored lines), for all cases in the MSP. The τ values are indicated in a corner of each plot distinguished by different shades. The curves on the semi-log graphs have been shifted vertically from bottom for enhanced clarity. We observe the characteristic peaked leptokurtic shapes of PDFs up to certain threshold scales. Following the downward turbulent cascade image—evolution of PDFs from higher to lower scales, we notice the continuous deformation of the increment PDFs and a stronger

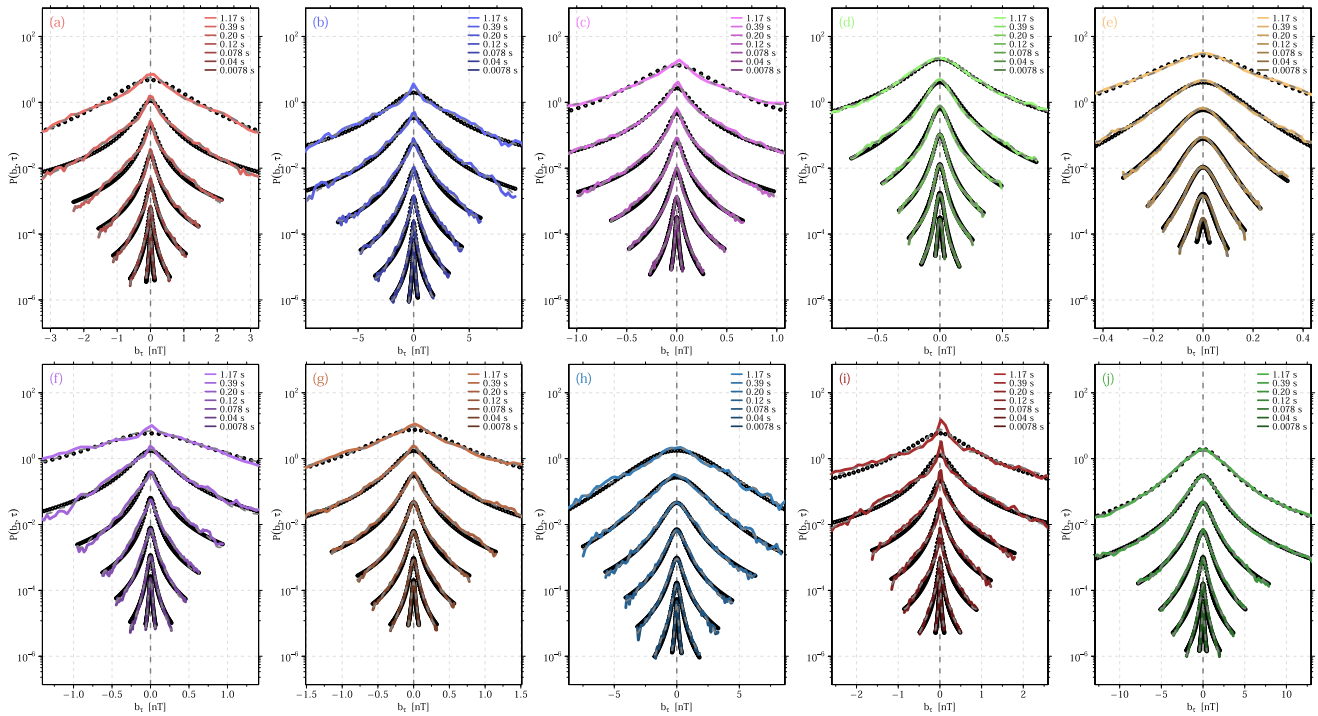

Figure 6. Empirical PDFs (colored lines) for a total strength of magnetic field $B = |\boldsymbol{B}|$ compared with the stationary (open circles) and non-stationary (gray dashed lines) solutions of the FP Equation 10 (shifted from bottom to top) for given time scales. Data in cases (a–j) corresponding to Tables 1 and 2.

deviation from the Gaussian PDFs. We see the non-Gaussian tails, which indicate intermittency in the time series structure. In cases *(b, f, i)* we see the pronounced peaks even for the highest available scales (compare Anvari, Lohmann, et al., 2016, Figures 2 and 6). This observation aligns with the prediction that the $\max\{P(b_\tau, \tau)\}$ become steeper for higher Re_λ, which results in a decrease of the coefficient $a_2(\tau)$ of Equation 15. For the remaining cases, for the highest scales τ_G, we see that the PDFs are rather Gaussian (as mathematically determined for large $\kappa \to \infty$). Complementarily, the kinetic-scale analyses of Wan et al. (2011, 2016) demonstrate a systematic increase in intermittency toward smaller scales, particularly ion- and electron-kinetic scales, indicated by increasing kurtosis and enhanced non-Gaussian statistics. Although operating in distinct scale regimes, both sets of results emphasize the complex and scale-dependent interplay of Gaussian and non-Gaussian behaviors inherent to plasma turbulence. We also observe fluctuations with "jumps," resulting in reduced smoothness in both theoretical and empirical curves, with smaller sample sizes exhibiting higher noise in fluctuations. Although, agreement between theoretical model predictions and observations is significant. To quantitatively evaluate it, we computed the Kolmogorov-Smirnov (KS) statistic between the FP solutions and observed PDFs. The KS statistics range from 0.02 to 0.06 across cases, all below the supposed critical value of $\alpha = 0.075$ confirming statistical agreement. Hence, these results indicate that the FP Equation 10 accurately describes the evolution of $P(b_\tau, \tau)$ on proposed scales in all considered cases of the MSP.

For consistency, we calculate values of the *symmetry* parameter λ for various scales and find that in all cases, it is approximately zero within the kinetic range. This is also illustrated in Figure 6, which shows that the PDFs are mostly symmetric about zero, and the tails have almost equal height. It suggests that the underlying energy transfer mechanisms operate equivalently in both directions of $\boldsymbol{B}$-field fluctuations. This testing also serves as a minor confirmation for the reduction of the generalized Kappa distribution.

5.6. Scale Invariance

In the study of solar wind turbulence, when PDFs get rescaled by their standard deviations, they often exhibit *scale invariance*, which is a sign of self-similar turbulent cascades (Benella et al., 2022; Macek et al., 2023). This invariance typically prevails up to a characteristic times scale, beyond which the PDFs transition toward Gaussian distributions, reflecting the dominance of large scale, less intermittent structures.

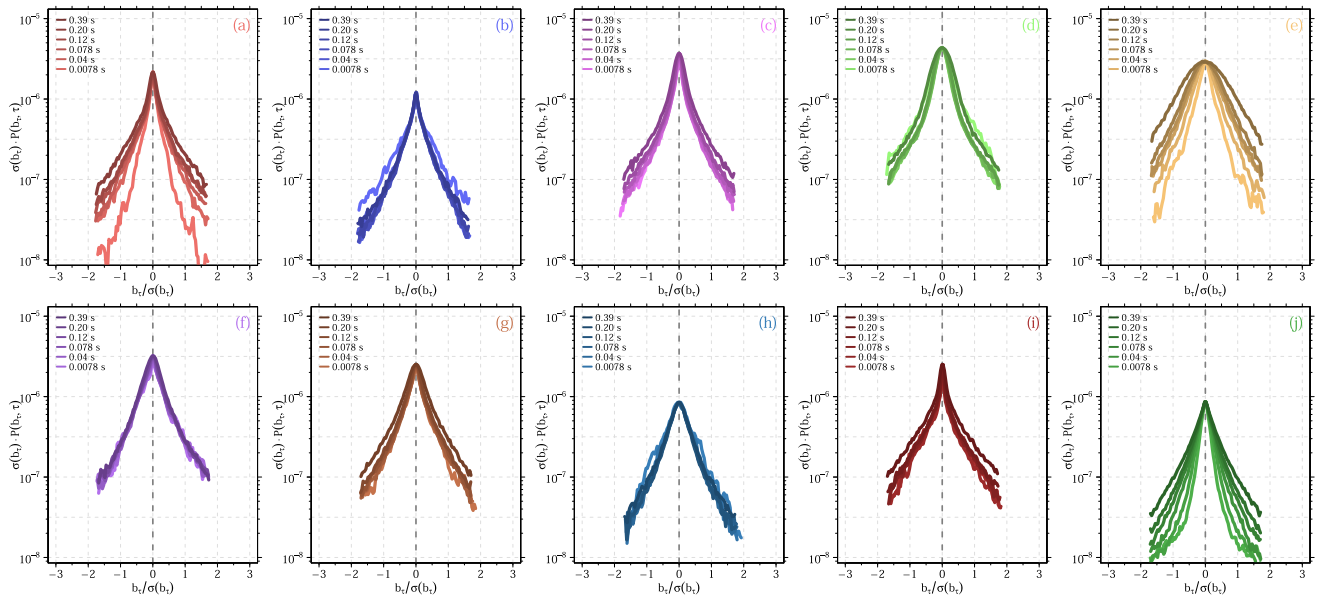

Figure 7. Rescaled empirical PDFs (colored lines) and the stationary solutions of the FP equations using magnetic field magnitude $B = |\boldsymbol{B}|$. We see the global scale invariance. Data in cases (a–j) corresponding to Tables 1 and 2.

In Figure 7, we depict the PDFs of fluctuations rescaled by their standard deviations $\sigma(b_\tau)$, that is, $b_\tau \to \frac{b_\tau}{\sigma(b_\tau)}$, and $P(b_\tau, \tau) \to \sigma(b_\tau)\, P(b_\tau, \tau)$, which define the *master curve* for the shape of the PDFs (Kiyani et al., 2009). In most cases, the curves are consistent with each other and with the stationary solutions (compare with Figure 6 open circles), at least up to approximately 0.4 s (see also Macek & Wójcik, 2023). For the larger τ values, the shapes become more smooth and gradually approach a Gaussian. For the lowest scale, that is, $\tau = 7.8$ ms, we cannot discern the regular *scale invariance*, although this observation aligns with the theory of the *Einstein-Markov scale* τ_{EM}, below which the Markov property does not hold for the turbulent cascade, rendering it of no interest (Lück et al., 2006). Furthermore, in cases *(e, j)* the strict *scale invariance* is not observed even within the appropriate Markovian range. This observation is significant, as these cases include the regions of the day-side EDR (reconnection jets). Conversely, for both night-side EDR (reconnection) regions, that is, cases *(f, g)*, we observe that this property is well satisfied, without any statistically significant deviations.

The slight breakdown of *scale invariance* in the day-side reconnection jet regions could be attributed to the complex dynamics inherent to magnetic reconnection processes, which leads to localized heating and particle acceleration. The contrasting behavior of day- and night-side EDRs, where electrons decouple from magnetic field lines, seem to stem from fundamental differences in their formation and plasma environments. Day-side reconnection occurs at the magnetopause where solar wind plasma directly interacts with the MSP, creating stronger density gradients, greater variability in plasma parameters, and more complex current sheet geometries. Night-side reconnection in the magnetotail occurs in a more homogeneous plasma environment with anti-parallel $\boldsymbol{B}$-field configurations. A few factors can contribute to the disruption of the *scale invariance* in day-side EDRs, for example, localized energy dissipation, anisotropic turbulence, or some nonstationary plasma conditions. Within the EDR, the reconnection process shows intense, localized energy conversion from magnetic to kinetic forms. This localized dissipation introduces structures that deviate from the typical turbulent cascade, thus breaking the expected scale invariance (Podesta & Borovsky, 2010). The reconnection process also induces anisotropies in plasma turbulence. Presence of strong guide fields and directional energy flows can lead to anisotropic distribution of turbulent fluctuations, which disrupts the self similar nature of the turbulence (Kiyani et al., 2009). In contrast, the night-side EDRs, located in magnetotail, often exhibit more stable plasma conditions with less direct influence from solar wind variations (Torbert et al., 2018). This relative stability allows the turbulent cascade to maintain its self-similarity, preserving scale invariance in the PDFs of the B-field fluctuations. Anyway, it seems that using a rescaled PDF analysis of the distinct scale invariance properties of day- and night-side reconnection regions could be a diagnostic tool for identifying reconnection types from the $\boldsymbol{B}$-field data. The exact mechanism

of generation of the magnetic fluctuation at these scales is still unknown, but empirical results suggest some clear universal characteristics of the processes.

6. Conclusions and Discussion

We have successfully extended the framework of Markovian processes to describe turbulent cascades across diverse magnetospheric (MSP) regions using *MMS* mission data. Our probabilistic approach establishes a clear distinction between multi-scale and multi-point statistics, with $(N + 1)$-point statistics represented by N-scale statistics (see also Peinke et al., 2019). Through hierarchical ordering of fluctuation statistics across time scales τ_i, we achieved 3-scale closure of N-scale statistics and validated Markovian properties of magnetic field fluctuations for scales $\tau > \tau_{EM}$ (Lück et al., 2006). Critically, we confirmed that the Markovian approximation depends on scale differences $(\tau - \tau')$ rather than their magnitude (e.g., $b_{\tau,i}$).

Using theory of Markov processes one can measure the differential equations describing evolution of cPDFs of the magnetic fluctuations with no model assumptions. This enables retrieval of stochastic equation for turbulent cascade straight from data. We have empirically evaluated the evolution equation for the cPDFs which is the Kramers-Moyal (KM) expansion in scale, that can be approximated by 2nd order Fokker-Planck (FP) equation in scale (or Langevin equation). The observed Markovian properties directly reflect the nature of energy transfer between scales in plasmas in MSP. The linearity of drift coefficients indicates relatively simple deterministic forcing mechanisms, while the quadratic diffusion coefficients suggest multiplicative stochastic processes consistent with intermittent structures forming at small scales. Comparison of the solutions of the Fokker-Planck equation with empirical samples supports the conclusions for the 1st and 2nd KM coefficients in scale. The Langevin noise is present, so the nonstationary solutions of the FP equation in scale are compared with empirical samples. We observe the varying shapes of the increment PDFs, which in a few cases are more pointy and have broader tails, that is a characteristic of higher internal *intermittency* (Tutkun & Mydlarski, 2004). The findings of observed intermittency in the MSP can be related to theoretical predictions by Mallet et al. (2016), Mallet and Schekochihin (2016). Authors explore how Alfvénic turbulence develops significant 3-D anisotropy and intermittency due to scale-dependent dynamic alignment of fluctuations and their nonlinear interactions. Our findings qualitatively align with their core conceptual descriptions. Their theory highlights how the intermittency phenomena and anisotropic scaling in plasma turbulence arise naturally from fundamental nonlinear plasma physics processes, and show the relevance of bridging statistical descriptions of turbulence and underlying plasma physical models. With our results, we wish to emphasize the fading boundary between the order and stochasticity in complex systems.

We provide novel dynamic intervals of the turbulent *MMS* data from around 2022–2023 including the EDR (reconnection) day- and night-side regions. These intervals can be compared with recently discovered unbiased *MMS* magnetosheath campaign from February 2023 by Pecora et al. (2025), which is a crucial near-Earth space region. Our discovered regions hold potential interest from a numerical, theoretical, and observational perspective for analyzing the relationship between the turbulence and the magnetic reconnection (see Stawarz et al., 2024).

Our analysis advances understanding of the intrinsic sub-range of turbulence, which is a well-known yet still unsolved physical problem. The *magnetic reconnection* is also important nonlinear phenomenon that remains unresolved, being a major objective of the *MMS* mission. Due to its rapidity, lasting mere tenths of a second, unprecedented time resolution is required. Thus, one should put more focus on the analysis of the turbulence in the EDRs, initiating magnetic reconnection, especially in a day-side of the MSP. We identified a crucial asymmetry between day-side and night-side reconnection regions: scale invariance breaks down in day-side EDRs (cases *(e, j)*) due to complex reconnection dynamics, while night-side regions maintain statistical self-similarity. With over 50 EDRs identified by *MMS* since 2015 (e.g., Macek et al., 2019b; Torbert et al., 2018; Webster et al., 2018, Macek et al., 2019a), machine learning approaches (e.g., Argall et al., 2020; Breuillard et al., 2020) now enable easier systematic investigations of these phenomena, particularly focusing on the rapid (sub-second) dynamics of day-side reconnection processes.

Conversely, the Markovian framework has inherent limitations for describing kinetic-scale turbulence. Formally, the analyzed stochastic processes are not purely Markovian due to the Einstein-Markov scale τ_{EM} and limited high-resolution data sets. The 2nd order FP approximation may oversimplify real turbulent PDFs, particularly for high-intermittency cases where higher-order Kramers-Moyal terms become significant. With increased internal

intermittency, the tails of PDFs become longer and more influential (Tutkun & Mydlarski, 2004). Regarding the Langevin equation, the process it models is not smooth, whereas turbulent quantities usually are, so approximating turbulent quantities will not yield exact solutions over all scales. It is related to δ-correlated forcing, but if this correlation does not occur, then the Markovianity is lost (Risken, 1996). Nevertheless, when modeling real-world physical phenomena one always needs certain more or less strict assumptions. Despite these constraints, this framework effectively captures essential turbulent cascade physics and internal intermittency effects in magnetic fields across the accessible scale range.

We note that it is still interesting to expand the scale-dependent stochastic Markov framework to higher dimensions and consider complex turbulent magnetic and velocity fields. Here, the $D^{(1)}(x_\tau, \tau)$ coefficient turns into a vector, while the $D^{(2)}(x_\tau, \tau)$ becomes a matrix. The extension to 2-D or 3-D spaces remains an open challenge, as the hierarchical turbulent downward cascade exhibits a clear ordering. Additionally, the future multi-spacecraft missions (HelioSwarm, Plasma Observatory, and MagCon) and even higher temporal resolution would enable 3-D validation of the stochastic properties and cascades identified here. Recent advances in multi-spacecraft turbulence diagnostics (Matthaeus et al., 2016; Pecora et al., 2023) could help us to extend the Markovian framework to spatially resolved processes, provided sufficient temporal continuity, for example, through mixed spatial-temporal Markovianity tests.

Data Availability Statement

The whole database supporting the results in this paper are available through the public *MMS* Science Data Center hosted by NASA (and co-hosted by the Laboratory for Atmospheric and Space Physics (LASP), University of Colorado, Boulder): http://cdaweb.gsfc.nasa.gov. However, to ensure reproducibility and transparency, the full data sets used in this publication are now publicly accessible also through Zenodo. Specifically, the data are available from (Wójcik & Macek, 2025).

All analyses and figures were generated using a combination of programming languages: *R* (version 4.4.0) (R Core Team, 2024), *Python* (version 3.10.13) (Python Software Foundation, 2021), and *Matlab* (version 25.1) (The MathWorks Inc, 2025) (and the libraries therein), as specified in the relevant subsections of this paper.

Acknowledgments

We acknowledge the pioneering work of R. Friedrich (1956–2012) on the theory of Markov properties employed to turbulence. We would like to thank the reviewers for their exhaustive and inspiring comments, which greatly improved our presentation. We are grateful for the dedicated efforts of the entire *MMS* mission team, with J. L. Burch, Principle Investigator, including development, science operations, and the Science Data Center at the Univ. of Colorado. We benefited from the efforts of T. E. Moore as Project Scientist, C. T. Russell, and the magnetometer team. We acknowledge Guan Le, MMS Project Scientist, for information about the magnetic field instrument, and also D. G. Sibeck and M. V. D. Silveira for discussions during previous visits by W. M. M. to the NASA Goddard Space Flight Center. This work has been supported by the National Science Centre, Poland (NCN) through Grant 2021/41/B/ST10/00823.

References

Afshari, A. S., Howes, G. G., Shuster, J. R., Klein, K. G., McGinnis, D., Martinović, M. M., et al. (2024). Direct observation of ion cyclotron damping of turbulence in Earth's magnetosheath plasma. *Nature Communications*, *15*(1), 7870. https://doi.org/10.1038/s41467-024-52125-8

Akaike, H. (1973). Information theory and an extension of the maximum likelihood principle. In B. N. Petrov & F. Csaki (Eds.), *Proceedings 2nd international symposium on information theory* (pp. 267–281). Akademiai Kiado. https://doi.org/10.1007/978-1-4612-1694-0_15

Alexandrova, O., Carbone, V., Veltri, P., & Sorriso-Valvo, L. (2008). Small-scale energy cascade of the solar wind turbulence. *The Astrophysical Journal*, *674*(2), 1153–1157. https://doi.org/10.1086/524056

Anvari, M., Lohmann, G., Wächter, M., Milan, P., Lorenz, E., Heinemann, D., et al. (2016). Short term fluctuations of wind and solar power systems. *New Journal of Physics*, *18*(6), 063027. https://doi.org/10.1088/1367-2630/18/6/063027

Anvari, M., Tabar, M., Peinke, J., & Lehnertz, K. (2016). Disentangling the stochastic behavior of complex time series. *Scientific Reports*, *6*(35435), 35435. https://doi.org/10.1038/srep35435

Argall, M. R., Small, C. R., Piatt, S., Breen, L., Petrik, M., Kokkonen, K., et al. (2020). MMS SITL ground loop: Automating the burst data selection process. *Frontiers in Astronomy and Space Sciences*, *7*, 54. https://doi.org/10.3389/fspas.2020.00054

Arzamasskiy, L., Kunz, M. W., Squire, J., Quataert, E., & Schekochihin, A. A. (2023). Kinetic turbulence in collisionless high-β plasmas. *Physical Review X*, *13*(2), 021014. https://doi.org/10.1103/PhysRevX.13.021014

AstroPy, Price-Whelan, A. M., Lim, P. L., Earl, N., Starkman, N., Bradley, L., et al. (2022). The Astropy Project: Sustaining and growing a community-oriented open-source project and the latest major release (v5.0) of the core package. *The Astrophysical Journal*, *935*(2), 167. https://doi.org/10.3847/1538-4357/ac7c74

Belardinelli, D., Benella, S., Stumpo, M., & Consolini, G. (2024). Derivation of a generalized kappa distribution from the scaling properties of solar wind magnetic field fluctuations at kinetic scales. *A&A*, *690*, A381. https://doi.org/10.1051/0004-6361/202450714

Benella, S., Stumpo, M., Alberti, T., Pezzi, O., Papini, E., Yordanova, E., et al. (2023). Linking the Langevin equation to scaling properties of space plasma turbulence at sub-ion scales. *Physical Review Research*, *5*(4), L042014. https://doi.org/10.1103/PhysRevResearch.5.L042014

Benella, S., Stumpo, M., Consolini, G., Alberti, T., Carbone, V., & Laurenza, M. (2022). Markovian features of the solar wind at subproton scales. *The Astrophysical Journal Letters*, *928*(2), L21. https://doi.org/10.3847/2041-8213/ac6107

Biskamp, D. (2003). *Magnetohydrodynamic turbulence*. Cambridge University Press. Retrieved from. https://doi.org/10.1017/CBO9780511535222

Bott, A. F. A., Kunz, M. W., Quataert, E., Squire, J., & Arzamasskiy, L. (2025). Thermodynamics and collisionality in firehose-susceptible high-β plasmas. Retrieved from https://arxiv.org/abs/2501.13663

Breuillard, H., Dupuis, R., Retino, A., Le Contel, O., Amaya, J., & Lapenta, G. (2020). Automatic classification of plasma regions in near-Earth space with supervised machine learning: Application to Magnetospheric Multi scale 2016–2019 observations. *Frontiers in Astronomy and Space Sciences*, *7*, 55. https://doi.org/10.3389/fspas.2020.00055

Bruno, R., & Carbone, V. (2013). The solar wind as a turbulence laboratory. *Living Reviews in Solar Physics*, *10*(1), 2. https://doi.org/10.12942/lrsp-2013-2

Bruno, R., & Carbone, V. (2016). *Turbulence in the solar wind* (Vol. 928). Springer International Publishing. https://doi.org/10.1007/978-3-319-43440-7

Burch, J. L., Giles, B. L., Ahmadi, N., Argall, M. R., Baker, D. N., Blake, J. B., et al. (2024). Magnetospheric Multiscale (MMS) - Calibration and measurement algorithms document (CMAD). *Space Physics Data Facility*. https://doi.org/10.48322/VSHD-SV21

Burch, J. L., Moore, T. E., Torbert, R. B., & Giles, B. L. (2016). Magnetospheric Multiscale overview and science objectives. *Space Science Reviews*, *199*(1–4), 5–21. https://doi.org/10.1007/s11214-015-0164-9

Burlaga, L. F. (1995). *Interplanetary magnetohydrodynamics*. Oxford University Press.

Chang, T. T. S. (2015). *An introduction to space plasma complexity*. Cambridge University Press.

Chen, B., & Hong, Y. (2012). Testing for the Markov property in time series. *Econometric Theory*, *28*(1), 130–178. https://doi.org/10.1017/s0266466611000065

Chen, C. H. K., Klein, K. G., & Howes, G. G. (2019). Evidence for electron Landau damping in space plasma turbulence. *Nature Communications*, *10*(1), 740. https://doi.org/10.1038/s41467-019-08435-3

Chen, C. H. K., Leung, L., Boldyrev, S., Maruca, B. A., & Bale, S. D. (2014). Ion-scale spectral break of solar wind turbulence at high and low beta. *Geophysical Research Letters*, *41*(22), 8081–8088. https://doi.org/10.1002/2014GL062009

Chen, F. F. (2016). *Introduction to plasma physics and controlled fusion* (3rd ed.). Springer. https://doi.org/10.1007/978-3-319-22309-4

Chollet, F., et al. (2015). Keras. Retrieved from https://keras.io

Davidson, P. (2015). *Turbulence: An introduction for scientists and engineers*. Oxford University Press. Retrieved from https://books.google.pl/books?id=VblDCQAAQBAJ

Echim, M., Chang, T., Kovacs, P., Wawrzaszek, A., Yordanova, E., Narita, Y., et al. (2021). Turbulence and complexity of magnetospheric plasmas. In *Magnetospheres in the solar system* (pp. 67–91). American Geophysical Union (AGU). https://doi.org/10.1002/9781119815624.ch5

Ewart, R. J., Nastac, M. L., Bilbao, P. J., Silva, T., Silva, L. O., & Schekochihin, A. A. (2025). Relaxation to universal non-maxwellian equilibria in a collisionless plasma. *Proceedings of the National Academy of Sciences*, *122*(17), e2417813122. https://doi.org/10.1073/pnas.2417813122

Friedrich, J. (2017). Closure of the Lundgren-Monin-Novikov hierarchy in turbulence via a Markov property of velocity increments in scale (Unpublished doctoral dissertation). Ruhr-Universität Bochum, Universitätsbibliothek.

Friedrich, R., & Peinke, J. (1997). Description of a turbulent cascade by a Fokker-Planck equation. *Physical Review Letters*, *78*(5), 863–866. https://doi.org/10.1103/PhysRevLett.78.863

Friedrich, R., Peinke, J., Sahimi, M., & Reza Rahimi Tabar, M. (2011). Approaching complexity by stochastic methods: From biological systems to turbulence. *Physics Reports*, *506*(5), 87–162. https://doi.org/10.1016/j.physrep.2011.05.003

Friedrich, R., Zeller, J., & Peinke, J. (1998). A note on three-point statistics of velocity increments in turbulence. *Europhysics Letters*, *41*(2), 153–158. https://doi.org/10.1209/epl/i1998-00124-7

Frisch, U. (1995). *Turbulence. The legacy of A.N. Kolmogorov*. Cambridge University Press. https://doi.org/10.1017/CBO9781139170666

Fuchs, A., Kharche, S., Patil, A., Friedrich, J., Wächter, M., & Peinke, J. (2022). An open source package to perform basic and advanced statistical analysis of turbulence data and other complex systems. *Physics of Fluids*, *34*(10), 101801. https://doi.org/10.1063/5.0107974

Grimes, E., Harter, B., Hatzigeorgiu, N., Drozdov, A., Lewis, J., Angelopoulos, V., et al. (2022). The space physics environment data analysis system in python. *Frontiers in Astronomy and Space Sciences*, *9*, 1020815. https://doi.org/10.3389/fspas.2022.1020815

Holstein, D., & Kantz, H. (2009). Optimal Markov approximations and generalized embeddings. *Physical Review E - Statistical Physics, Plasmas, Fluids, and Related Interdisciplinary Topics*, *79*(5), 056202. https://doi.org/10.1103/PhysRevE.79.056202

Honisch, C., & Friedrich, R. (2011). Estimation of Kramers-Moyal coefficients at low sampling rates. *Physical Review E - Statistical Physics, Plasmas, Fluids, and Related Interdisciplinary Topics*, *83*(6), 066701. https://doi.org/10.1103/PhysRevE.83.066701

Howes, G. G. (2024). The fundamental parameters of astrophysical plasma turbulence and its dissipation: Non-relativistic limit. *Journal of Plasma Physics*, *90*(5), 905900504. https://doi.org/10.1017/S0022377824001090

Howes, G. G., Cowley, S. C., Dorland, W., Hammett, G. W., Quataert, E., & Schekochihin, A. A. (2008). A model of turbulence in magnetized plasmas: Implications for the dissipation range in the solar wind. *Journal of Geophysical Research: Space Physics*, *113*(A5). https://doi.org/10.1029/2007JA012665

Howes, G. G., Klein, K. G., & TenBarge, J. M. (2014). Validity of the Taylor hypothesis for linear kinetic waves in the weakly collisional solar wind. *The Astrophysical Journal*, *789*(2), 106. https://doi.org/10.1088/0004-637X/789/2/106

Ibragimov, R. (2009). Copula-based characterizations for higher order Markov processes. *Econometric Theory*, *25*(3), 819–846. https://doi.org/10.1017/S0266466609090720

Kiyani, K. H., Chapman, S. C., Khotyaintsev, Y. V., Dunlop, M. W., & Sahraoui, F. (2009). Global scale-invariant dissipation in collisionless plasma turbulence. *Physical Review Letters*, *103*(7), 075006. https://doi.org/10.1103/PhysRevLett.103.075006

Klein, K. G., Howes, G. G., & TenBarge, J. M. (2014). The violation of the Taylor hypothesis in measurements of solar wind turbulence. *The Astrophysical Journal Letters*, *790*(2), L20. https://doi.org/10.1088/2041-8205/790/2/L20

Kolmogorov, A. N. (1941). The local structure of turbulence in incompressible viscous fluid for very large Reynolds' numbers. *Doklady Akademii Nauk SSSR*, *30*, 301–305.

Kolmogorov, A. N. (1962). A refinement of previous hypotheses concerning the local structure of turbulence in a viscous incompressible fluid at high Reynolds number. *Journal of Fluid Mechanics*, *13*(1), 82–85. https://doi.org/10.1017/s0022112062000518

Landau, L., & Lifshitz, E. (1987). *Fluid Mechanics* (Vol. 6). Butterworth-Heinemann. Retrieved from https://books.google.pl/books?id=eVKbCgAAQBAJ

Laval, J.-P., & Dubrulle, B. (2006). A LES-Langevin model for turbulence. *European Physical Journal B: Condensed Matter and Complex Systems*, *49*(4), 471–481. https://doi.org/10.1140/epjb/e2006-00082-4

Laval, J.-P., Dubrulle, B., & Nazarenko, S. (2001). Nonlocality and intermittency in three-dimensional turbulence. *Physics of Fluids*, *13*(7), 1995–2012. https://doi.org/10.1063/1.1373686

Leamon, R. J., Smith, C. W., Ness, N. F., Matthaeus, W. H., & Wong, H. K. (1998). Observational constraints on the dynamics of the interplanetary magnetic field dissipation range. *Journal of Geophysical Research: Space Physics*, *103*(A3), 4775–4787. https://doi.org/10.1029/97JA03394

Lehle, B. (2011). Analysis of stochastic time series in the presence of strong measurement noise. *Physical Review E - Statistical Physics, Plasmas, Fluids, and Related Interdisciplinary Topics*, *83*(2), 021113. https://doi.org/10.1103/PhysRevE.83.021113

Lück, S., Renner, C., Peinke, J., & Friedrich, R. (2006). The Markov–Einstein coherence length—A new meaning for the Taylor length in turbulence. *Physics Letters A*, *359*(5), 335–338. https://doi.org/10.1016/j.physleta.2006.06.053

Macek, W. M., Silveira, M. V. D., Sibeck, D. G., Giles, B. L., & Burch, J. L. (2019a). Magnetospheric MultiscaleMission Observations of Reconnecting Electric Fields in the Magnetotail on Kinetic Scales.*Geophysical Research Letters*, *46*(17–18), 10295–10302. https://doi.org/10.1029/2019gl083782

Macek, W. M., Silveira, M. V. D., Sibeck, D. G., Giles, B. L., & Burch, J. L. (2019b). Mechanism of reconnection on kinetic scales based on Magnetospheric Multiscale mission observations. *The Astrophysical Journal Letters*, *885*(1), L26. https://doi.org/10.3847/2041-8213/ab4b5a

Macek, W. M., & Wójcik, D. (2023). Statistical analysis of stochastic magnetic fluctuations in space plasma based on the MMS Mission. *Monthly Notices of the Royal Astronomical Society*, *526*(4), 5779–5790. https://doi.org/10.1093/mnras/stad2584

Macek, W. M., Wójcik, D., & Burch, J. L. (2023). Magnetospheric Multiscale observations of Markov turbulence on kinetic scales. *The Astrophysical Journal*, *943*(2), 152. https://doi.org/10.3847/1538-4357/aca0a0

Mallet, A., & Schekochihin, A. A. (2016). A statistical model of three-dimensional anisotropy and intermittency in strong Alfvénic turbulence. *Monthly Notices of the Royal Astronomical Society*, *466*(4), 3918–3927. https://doi.org/10.1093/mnras/stw3251

Mallet, A., Schekochihin, A. A., Chandran, B. D. G., Chen, C. H. K., Horbury, T. S., Wicks, R. T., & Greenan, C. C. (2016). Measures of three-dimensional anisotropy and intermittency in strong Alfvénic turbulence. *Monthly Notices of the Royal Astronomical Society*, *459*(2), 2130–2139. https://doi.org/10.1093/mnras/stw802

Marcq, P., & Naert, A. (2001). A Langevin equation for turbulent velocity increments. *Physics of Fluids*, *13*(9), 2590–2595. https://doi.org/10.1063/1.1386937

Matthaeus, W. H. (2021). Turbulence in space plasmas: Who needs it? *Physics of Plasmas*, *28*(3), 032306. https://doi.org/10.1063/5.0041540

Matthaeus, W. H., Weygand, J. M., Chuychai, P., Dasso, S., Smith, C. W., & Kivelson, M. G. (2008). Interplanetary magnetic Taylor microscale and implications for plasma dissipation. *The Astrophysical Journal*, *678*(2), L141–L144. https://doi.org/10.1086/588525

Matthaeus, W. H., Weygand, J. M., & Dasso, S. (2016). Ensemble space-time correlation of plasma turbulence in the solar wind. *Physical Review Letters*, *116*(24), 245101. https://doi.org/10.1103/PhysRevLett.116.245101

Matthaeus, W. H., Zank, G. P., Smith, C. W., & Oughton, S. (1999). Turbulence, spatial transport, and heating of the solar wind. *Physical Review Letters*, *82*(17), 3444–3447. https://doi.org/10.1103/PhysRevLett.82.3444

Nawroth, A., & Peinke, J. (2006). Multiscale reconstruction of time series. *Physics Letters A*, *360*(2), 234–237. https://doi.org/10.1016/j.physleta.2006.08.024

Nawroth, A. P., Friedrich, R., & Peinke, J. (2010). Multi-scale description and prediction of financial time series. *New Journal of Physics*, *12*(8), 083021. https://doi.org/10.1088/1367-2630/12/8/083021

Nickelsen, D., & Engel, A. (2013). Probing small-scale intermittency with a fluctuation theorem. *Physical Review Letters*, *110*(21), 214501. https://doi.org/10.1103/PhysRevLett.110.214501

Pavlos, G., Karakatsanis, L., Xenakis, M., Sarafopoulos, D., & Pavlos, E. (2012). Tsallis statistics and magnetospheric self-organization. *Physica A: Statistical Mechanics and its Applications*, *391*(11), 3069–3080. https://doi.org/10.1016/j.physa.2012.01.0

Pecora, F., Chhiber, R., Chasapis, A., Vo, T., Sorriso-Valvo, L., Montagud-Camps, V., & Matthaeus, W. (2025). *General properties of the magnetosheath: The MMS unbiased campaign*. ESS Open Archive. https://doi.org/10.22541/essoar.173939561.16950895/v1

Pecora, F., Yang, Y., Matthaeus, W. H., Chasapis, A., Klein, K. G., Stevens, M., et al. (2023). Three-dimensional energy transfer in space plasma turbulence from multipoint measurement. *Physical Review Letters*, *131*(22), 225201. https://doi.org/10.1103/PhysRevLett.131.225201

Peinke, J., Tabar, M., & Wächter, M. (2019). The Fokker–Planck approach to complex spatiotemporal disordered systems [Journal Article]. *Annual Review of Condensed Matter Physics*, *10*(2019), 107–132. https://doi.org/10.1146/annurev-conmatphys-033117-054252

PlasmaPy, C., Murphy, N. A., Everson, E. T., Stańczak-Marikin, D., Heuer, P. V., Kozlowski, P. M., et al. (2024). Plasmapy. *Zenodo*. https://doi.org/10.5281/zenodo.14010450

Podesta, J. J., & Borovsky, J. E. (2010). Scale invariance of normalized cross-helicity throughout the inertial range of solar wind turbulence. *Physics of Plasmas*, *17*(11), 112905. https://doi.org/10.1063/1.3505092

Python Software Foundation. (2021). Python Language reference [Software]. https://www.python.org

R Core Team. (2024). R: A language and environment for statistical computing [Computer software manual]. https://www.R-project.org/

Reinke, N., Fuchs, A., Nickelsen, D., & Peinke, J. (2018). On universal features of the turbulent cascade in terms of non-equilibrium thermodynamics. *Journal of Fluid Mechanics*, *848*, 117–153. https://doi.org/10.1017/jfm.2018.360

Renner, C., Peinke, J., & Friedrich, R. (2001). Experimental indications for Markov properties of small-scale turbulence. *Journal of Fluid Mechanics*, *433*, 383–409. https://doi.org/10.1017/S0022112001003597

Richardson, L. F. (1920). *Weather prediction by numerical process* (2nd ed.). Cambridge University Press.

Risken, H. (1996). *The Fokker-Planck equation: Methods of solution and applications*. Springer Berlin Heidelberg. Retrieved from https://books.google.pl/books?id=MG2V9vTgSgEC

Roberts, O. W., Klein, K. G., Vörös, Z., Nakamura, R., Li, X., Narita, Y., et al. (2024). Measurement of the Taylor microscale and the effective magnetic Reynolds number in the solar wind with Cluster. *Journal of Geophysical Research: Space Physics*, *129*(11), e2024JA032968. https://doi.org/10.1029/2024JA032968

Roy, S., Bandyopadhyay, R., Yang, Y., Parashar, T. N., Matthaeus, W. H., Adhikari, S., et al. (2022). Turbulent energy transfer and proton–electron heating in collisionless plasmas. *The Astrophysical Journal*, *941*(2), 137. https://doi.org/10.3847/1538-4357/aca479

Sahraoui, F., Goldstein, M. L., Robert, P., & Khotyaintsev, Y. V. (2009). Evidence of a cascade and dissipation of solar-wind turbulence at the electron Gyroscale. *Physical Review Letters*, *102*(23), 231102. https://doi.org/10.1103/PhysRevLett.102.231102

Schekochihin, A. A., Cowley, S. C., Dorland, W., Hammett, G. W., Howes, G. G., Quataert, E., & Tatsuno, T. (2009). Astrophysical gyrokinetics: Kinetic and fluid turbulent cascades in magnetized weakly collisional plasmas. *The Astrophysical Journal Supplement*, *182*(1), 310–377. https://doi.org/10.1088/0067-0049/182/1/310

Schwarz, G. (1978). Estimating the dimension of a model. *Annals of Statistics*, *6*(2), 461–464. https://doi.org/10.1214/aos/1176344136

Shi, C., Wan, R., Song, R., Lu, W., & Leng, L. (2020). Does the Markov decision process fit the data: Testing for the Markov property in sequential decision making. Retrieved from https://arxiv.org/abs/2002.01751

Small, C., Argall, M., & Petrik, M. (2020). GLS-MP: Automated magnetopause crossing detection. Retrieved from https://github.com/colinrsmall/GLS-MP

Small, C. R., Argall, M. R., & Petrik, M. (2020). MMS SITL ground loop: Notebooks to train and run the GLS-Mp model. *Zenodo*. https://doi.org/10.5281/zenodo.3891992

Sreenivasan, K. R. (2004). Possible effects of small-scale intermittency in turbulent reacting flows. *Flow, Turbulence and Combustion*, *72*(2), 115–131. https://doi.org/10.1023/B:APPL.0000044408.46141.26

Stawarz, J. E., Muñoz, P. A., Bessho, N., Bandyopadhyay, R., Nakamura, T. K. M., Eriksson, S., et al. (2024). The interplay between collisionless magnetic reconnection and turbulence. *Space Science Reviews*, *220*(8), 90. https://doi.org/10.1007/s11214-024-01124-8

Stresing, R., & Peinke, J. (2010). Towards a stochastic multi-point description of turbulence. *New Journal of Physics*, *12*(10), 103046. https://doi.org/10.1088/1367-2630/12/10/103046

Strumik, M., & Macek, W. M. (2008a). Statistical analysis of transfer of fluctuations in solar wind turbulence. *Nonlinear Processes in Geophysics*, *15*(4), 607–613. https://doi.org/10.5194/npg-15-607-2008

Strumik, M., & Macek, W. M. (2008b). Testing for Markovian character and modeling of intermittency in solar wind turbulence. *Physical Review E - Statistical Physics, Plasmas, Fluids, and Related Interdisciplinary Topics*, *78*(2), 026414. https://doi.org/10.1103/PhysRevE.78.026414

Tabar, M. (2019). *Analysis and data-based reconstruction of complex nonlinear dynamical systems: Using the methods of stochastic processes*. Springer. https://doi.org/10.1007/978-3-030-18472-8

Taylor, G. I. (1938). The spectrum of turbulence. *Proceedings of the Royal Society of London. Series A-Mathematical and Physical Sciences*, *164*(919), 476–490. https://doi.org/10.1098/rspa.1938.0032

The MathWorks Inc. (2025). *Matlab version: 25.1.0.2943329 (r2025a)*. The MathWorks Inc. Retrieved from https://www.mathworks.com/

Torbert, R. B., Burch, J. L., Phan, T. D., Hesse, M., Argall, M. R., Shuster, J., et al. (2018). Electron-scale dynamics of the diffusion region during symmetric magnetic reconnection in space. *Science*, *362*(6421), 1391–1395. https://doi.org/10.1126/science.aat2998

Torbert, R. B., Russell, C. T., Magnes, W., Ergun, R. E., Lindqvist, P. A., Le Contel, O., et al. (2016). The FIELDS instrument suite on MMS: Scientific objectives, measurements, and data products. *Space Science Reviews*, *199*(1–4), 105–135. https://doi.org/10.1007/s11214-014-0109-8

Tsallis, C. (1988). Possible generalization of Boltzmann-Gibbs statistics. *Journal of Statistical Physics*, *52*(1–2), 479–487. https://doi.org/10.1007/BF01016429

Tutkun, M., & Mydlarski, L. (2004). Markovian properties of passive scalar increments in grid-generated turbulence. *New Journal of Physics*, *6*(1), 49. https://doi.org/10.1088/1367-2630/6/1/049

Vech, D., Mallet, A., Klein, K. G., & Kasper, J. C. (2018). Magnetic reconnection may control the ion-scale spectral break of solar wind turbulence. *The Astrophysical Journal Letters*, *855*(2), L27. https://doi.org/10.3847/2041-8213/aab351

Verscharen, D., Klein, K. G., & Maruca, B. A. (2019). The multi-scale nature of the solar wind. *Living Reviews in Solar Physics*, *16*(1), 5. https://doi.org/10.1007/s41116-019-0021-0

Wan, M., Matthaeus, W. H., Roytershteyn, V., Parashar, T. N., Wu, P., & Karimabadi, H. (2016). Intermittency, coherent structures and dissipation in plasma turbulence. *Physics of Plasmas*, *23*(4), 042307. https://doi.org/10.1063/1.4945631

Wan, M., Osman, K. T., Matthaeus, W. H., & Oughton, S. (2011). Investigation of intermittency in magnetohydrodynamics and solar wind turbulence: Scale-dependent kurtosis. *The Astrophysical Journal*, *744*(2), 171. https://doi.org/10.1088/0004-637X/744/2/171

Webster, J. M., Burch, J. L., Reiff, P. H., Daou, A. G., Genestreti, K. J., Graham, D. B., et al. (2018). Magnetospheric Multiscale dayside reconnection electron diffusion region events. *Journal of Geophysical Research: Space Physics*, *123*(6), 4858–4878. https://doi.org/10.1029/2018JA025245

Weygand, J. M., Matthaeus, W. H., Dasso, S., Kivelson, M. G., Kistler, L. M., & Mouikis, C. (2009). Anisotropy of the Taylor scale and the correlation scale in plasma sheet and solar wind magnetic field fluctuations. *Journal of Geophysical Research: Space Physics*, *114*(A7). https://doi.org/10.1029/2008JA013766

Wicks, R. T., Horbury, T. S., Chen, C. H. K., & Schekochihin, A. A. (2010). Power and spectral index anisotropy of the entire inertial range of turbulence in the fast solar wind. *Monthly Notices of the Royal Astronomical Society: Letters*, *407*(1), L31–L35. https://doi.org/10.1111/j.1745-3933.2010.00898.x

Wójcik, D., & Macek, W. M. (2024). Testing for Markovian character of transfer of fluctuations in solar wind turbulence on kinetic scales. *Physical Review E - Statistical Physics, Plasmas, Fluids, and Related Interdisciplinary Topics*, *110*(2), 025203. https://doi.org/10.1103/PhysRevE.110.025203

Wójcik, D., & Macek, W. M. (2025). Searching for universality of turbulence in the Earth's magnetosphere datasets [Dataset]. *Zenodo*. https://doi.org/10.5281/zenodo.16421681

Zhdankin, V. (2023). Dimensional measures of generalized entropy. *Journal of Physics A: Mathematical and Theoretical*, *56*(38), 385002. https://doi.org/10.1088/1751-8121/acf175